Interaction of Short X-ray Pulses with Small Molecules

Diplomarbeit

vorgelegt von

Carl Friedrich Burmeister

aus Braunschweig

Göttingen, den 6 Juli 2009

Department for Theoretical and Computational Biophysics

Max Planck Institute for Biophysical Chemistry, Göttingen

Contents

1 Introduction

X-ray crystallography is the state of the art method to obtain atomic resolution structures of large biomolecules such as proteins. The method has been known for almost a century and was first applied to proteins in the fifties. Max Perutz and John Kendrew were awarded with the Nobel prize in 1962 for solving the first protein structure with X-ray crystallography [1]. To use X-ray crystallography, a crystal of the target molecule is needed. The formation of such crystals is the major challenge for application of X-ray crystallography to proteins. Many protein structures are still unknown because no one has been able to crystallize them.

One reason for using crystals is to overcome the radiation damage. With current X-ray source it is no possible to use a single molecule scattering experiments for structure determination because the molecule is destroyed by the radiation before a useful amount of data was acquired. The crystal provides a large ensemble of molecules over which the radiation damage is distributed. The recorded signal is an average over the whole ensemble. Thus the effect of the destruction of single molecules on the final data is small. The regular arrangement of the molecules in the crystal allows the extraction of the molecular structure.

A new generation of X-ray source holds the promise to overcome this problem.

The free electron laser based X-ray lasers currently being built in Germany, Japan and the USA will become available within the next years. The ultra short (less then 100 fs) and ultra intense (more then 10^{11}photons/pulse) pulses offer the possibility to use single molecule scattering for structure determination of large molecules, which would circumvent the need to grow protein crystals and holds the promise to achieve atomic resolution [2].

In this approach the data is gathered form images of individual molecules. Each of these molecules will be destroyed in an explosion caused by the radiation. The pulse length and the length of the explosion are of the same order of magnitude. Thus it might be possible to obtain enough data from each molecule before it is destroyed. To predict the pulse length needed to achieve atomic resolution with this method, it is crucial to know, how fast this destruction takes place. Biological samples are mainly composed of light elements. The interaction of X-ray radiation of about 0.1 nm with light elements is dominated by three processes, the photoelectric effect, elastic and inelastic scattering (see figure 1.1). Ionisation

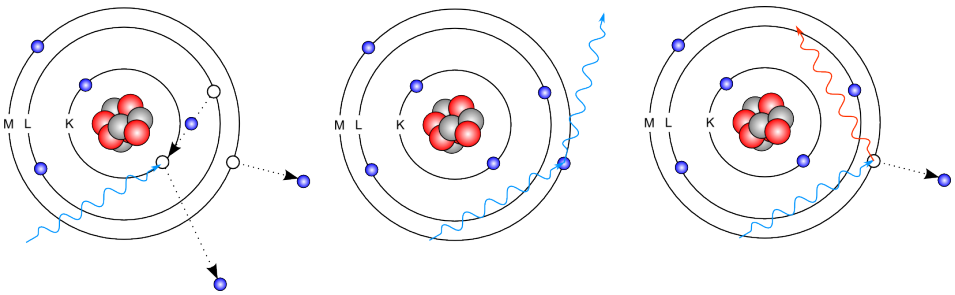

Figure 1.1: Sketch of the Auger effect (left), elastic scattering (middle) and inelastic scattering (right)

of a K shell electron is the most probable process. This leaves the molecule in an excited state, that decays mainly via the Auger effect causing a second electron to be ejected from the sample. Together with the intensity of the pulse this lead to a major fraction of the electrons of the sample being stripped of. The loss of covalent bonds and the high positive charge causes the explosion of the sample.

This process is therefore called the Coulomb explosion.

Several attempts have been made to study the Coulomb explosion with computer simulation. A study carried out by Stefan Hau-Riege and coworkers [3] used a one dimensional model for both the nuclei and the electrons. The different ion species are treated as number densities and the electrons as a free electron gas. A stochastic criterion based on atomic (ionic) ionisation cross-sections and the flux of the laser pulse was used to model the photoemission. The secondary electronic processes including the Auger effect and collisional ionisation from escaping electrons were described by rate equations. The most important result is that the explosion of the inner part of the sample is hampered. Quasi free electrons are trapped by the spherical charge distribution during later stages of the explosion effectively neutralise the inner part of the sample. This effect might play an important role for the stability of the target molecule, since in the experiment it will be enclosed in a water droplet.

Richard Neutze and coworkers [2] used a modified molecular dynamics simulation. Again the photoionization is modeled with a stochastic criterion. The probability of an atom being ionized is estimated by its photoionization cross-section and the number of photons passing the according area. The Auger decay is assumed to be an exponential decay with the life time according to atomic data. Ejected electrons were assumed to always leave the sample. Thus the explosion of the inner part of the sample could not be observed. The first atoms to leave the molecule are hydrogens and sulphurs, the latter being highly ionized due to their large photoionization cross-section and short Auger life times.

Both approaches involve severe approximations. In the first study it is assumed that the electrostatic interaction dominates nuclei-nuclei interaction completely. The effect of covalent bonds is neglected. Although this approximation is reasonable for the later part of the explosion, it is certainly very crude for the first part when only a small part of the molecule is ionized. The latter study relies on a force field. The force fields used in molecular dynamics simulations are param-

eterized with respect to the electronic ground state. Accordingly both studies neglect the effect of the changing electronic wave function on the nuclear dynamics. However, during the early phase of the explosion the nuclear dynamics will be determined by the electronic wave function.

Thus it is necessary to provide a more accurate description of the electronic dynamics and of its effect on the motion of the nuclei. A recent study shows [4] that it is possible to track the electronic processes following an instantaneous ionization of the K hell of a rare gas dimer by using a correlated post-Hartree-Fock method. However, the systems of interest here are much larger. The aim of this thesis is therefore to describe electronic processes following K shell ionisation by employing the time-dependent Hartree-Fock theory.

2

Hartree-Fock theory

In this chapter a way to approximatively solve the Schrödinger equation is presented. The necessary concepts are introduced with respect to the stationary equation and then extended to the time-dependent equation.
The solution of the stationary Schrödinger equation

$$\begin{aligned}\hat{H}\Psi(\{\mathbf{R}_A\},\{\mathbf{r}_j\}) &= E\Psi(\{\mathbf{R}_A\},\{\mathbf{r}_j\})\\ \hat{H} = &-\sum_A^M \frac{1}{2M_A}\Delta_A - \sum_j^N \frac{1}{2}\Delta_j + \\ &\sum_j^N\sum_A^M \frac{Z_A}{r_{jA}} + \sum_j^N\sum_{k>j}^N \frac{1}{r_{jk}} + \sum_A^M\sum_{B>A}^M \frac{Z_A Z_B}{R_{AB}},\end{aligned} \tag{2.1}$$

where N denotes the number of electrons, M the number of nuclei, r_{jk} the distance between the electrons j and k, r_{jA} the distance between electron j and nucleus A, R_{AB} the distance between nuclei A and B and Z_A and M_A the charge and mass of nucleus A, is for all, but the simplest, cases a many body problem. Thus there is, in general, no analytic solution. One therefore has to rely on approximations. Since biomolecules are mainly composed of first and second row elements, relativistic effects can be neglected. Accordingly, no spin dependence is included within the Hamiltonian. Another approximation commonly invoked in molecular physics is the Born-Oppenheimer approximation where the nuclear

degrees of freedom are separated from the electronic ones. This is reasonable since a nucleus is at least three orders of magnitude heavier then an electron. For calculations of the electronic wave function the nuclei are kept fixed. Therefore, the electronic wave function and energy depend only parametrically on the positions of the nuclei

$$\begin{aligned}\hat{H}_{elec}\Psi(\{\mathbf{r}_j\};\{\mathbf{R}_A\}) &= E_{elec}(\{\mathbf{R}_A\})\Psi(\{\mathbf{r}_j\};\{\mathbf{R}_A\}) \\ \hat{H}_{elec} &= -\sum_j^N \frac{1}{2}\Delta_j + \sum_j^N \sum_A^M \frac{Z_A}{r_{jA}} + \sum_j^N \sum_{k>j}^N \frac{1}{r_{jk}}. \end{aligned} \tag{2.2}$$

Due to the electron-electron repulsion, this is again an n-body problem for all but the simplest cases. Again, there is in general no analytic solution to this problem. One possibility to obtain an approximative solution is the Hartree-Fock theory. In Hartree-Fock Theory the wave function is represented as a single Slater determinate, which is an antisymmetrized product ansatz of single particle wave functions. Together with the mean field interaction of the electrons, this turns the n-body problem of the Schrödinger equation into n coupled 1-body problems.

In the subsequent section, the Hartree-Fock equations are derived using the above mentioned approximations and a variational principle. In the second section, it is shown how to solve the Hartree-Fock equation numerically by introducing a finite spatial basis set. In the last section, the (time-dependent) Dirac-Frenkel variational principle is used to derive the time-dependent Hartree-Fock equations using the same approximations as above.

2.1 Hartree-Fock equations

The wave function is constructed from a set of single particle wave functions $\{\chi_j(\mathbf{x})\}$ the spin orbitals, where $\mathbf{x} = \{\mathbf{r}, \omega\}$ denotes a combined space spin vari-

able. With these the Slater determinant can be formally written as

$$\Psi(\{\mathbf{x}_j\}) = \frac{1}{\sqrt{N!}} \begin{vmatrix} \chi_1(x_1) & \chi_2(x_1) & \dots & \chi_N(x_1) \\ \chi_1(x_2) & \chi_2(x_2) & \dots & \chi_N(x_2) \\ \vdots & \vdots & & \vdots \\ \chi_1(x_N) & \chi_2(x_N) & \dots & \chi_N(x_N) \end{vmatrix}. \tag{2.3}$$

To derive the Hartree-Fock equations, a variational principle is used. The spin orbitals are chose such that they minimize the electronic energy. That is,

$$E_{elec} = \langle \Psi | \hat{H}_{elec} | \Psi \rangle \tag{2.4}$$

is minimized with respect to the constraint, that the spin orbitals stay orthonormal

$$\langle \chi_j | \chi_k \rangle = \int \mathrm{d}\mathbf{x} \chi_j^*(\mathbf{x}) \chi_k(\mathbf{x}) = \delta_{jk}, \tag{2.5}$$

and otherwise arbitrary variations of the spin orbitals. Let

$$\hat{h}_j = -\frac{1}{2}\Delta_j + \sum_A^M \frac{Z_A}{r_{jA}} \tag{2.6}$$

be the one particle part of the Hamiltonian and

$$\langle \chi_j \chi_k | \frac{1}{r_{12}} | \chi_m \chi_n \rangle = \int \mathrm{d}\mathbf{x}_1 \mathrm{d}\mathbf{x}_2 \chi_j^*(\mathbf{x}_1) \chi_k^*(\mathbf{x}_2) \frac{1}{r_{12}} \chi_m(\mathbf{x}_1) \chi_n(\mathbf{x}_2). \tag{2.7}$$

The energy (2.4) can be interpreted as a functional of the orbitals. The above definitions together with (2.3) and (2.2) yield

$$\begin{aligned} E_{elec}[\{\chi_j\}] = & \sum_j^N \langle \chi_j | \hat{h}_j | \chi_j \rangle + \\ & \frac{1}{2} \sum_j^N \sum_k^N \langle \chi_k \chi_l | \frac{1}{r_{12}} | \chi_k \chi_l \rangle - \langle \chi_l \chi_k | \frac{1}{r_{12}} | \chi_k \chi_l \rangle. \end{aligned} \tag{2.8}$$

To deploy the variational principle, the Lagrangian

$$L[\{\chi_j\}] = E_{elec}[\{\chi_j\}] - \sum_j^N \sum_k^N \epsilon_{kj} (\langle \chi_j | \chi_k \rangle - \delta_{jk}) \tag{2.9}$$

is defined and

$$\delta L = \delta E - \sum_j^N \sum_k^N \epsilon_{kj} \delta(\langle \chi_j | \chi_k \rangle - \delta_{jk}) = 0 \tag{2.10}$$

is set. Performing the algebra leads to

$$\begin{aligned}
\delta L =& \sum_j^N \langle \delta\chi_j | \hat{h}_j | \chi_j \rangle + \\
& \frac{1}{2} \sum_j^N \sum_k^N \langle \delta\chi_j \chi_k | \frac{1}{r_{12}} | \chi_j \chi_k \rangle + \langle \chi_j \delta\chi_k | \frac{1}{r_{12}} | \chi_j \chi_k \rangle - \\
& \langle \delta\chi_k \chi_j | \frac{1}{r_{12}} | \chi_j \chi_k \rangle - \langle \chi_k \delta\chi_j | \frac{1}{r_{12}} | \chi_j \chi_k \rangle - \\
& - \epsilon_{kj} \langle \delta\chi_j | \chi_k \rangle + \text{complex conjugate} \\
=& 0 \\
\Rightarrow & \sum_j^N \int \mathrm{d}\mathbf{x}_1 \delta\chi_j^*(\mathbf{x}_1) \left\{ \hat{h}_j(\mathbf{x}_1) \chi_j(\mathbf{x}_1) + \sum_k^N \int \mathrm{d}\mathbf{x_2} \chi_k^*(\mathbf{x}_2) \chi_k(\mathbf{x}_2) \frac{1}{r_{12}} \chi_j(\mathbf{x}_1) \right. \\
& \left. - \int \mathrm{d}\mathbf{x}_2 \chi_k^*(\mathbf{x}_2) \frac{1}{r_{12}} \chi_j(\mathbf{x}_2) \chi_k(\mathbf{x}_1) \right\} - \sum_k^N \epsilon_{kj} \chi_k(\mathbf{x}_1) \\
=& \sum_j^N \int \mathrm{d}\mathbf{x}_1 \delta\chi_j^*(\mathbf{x}_1) \left\{ \hat{h}_j(\mathbf{x}_1) + \sum_k^N \hat{J}_k(\mathbf{x}_1) - \hat{K}_k(\mathbf{x}_1) \right\} \chi_j(\mathbf{x}_1) \\
=& 0,
\end{aligned} \tag{2.11}$$

with

$$\hat{J}_k(\mathbf{x}_1) \chi_j(\mathbf{x}_1) = \int \mathrm{d}\mathbf{x}_2 \chi_k^*(\mathbf{x}_2) \chi_k(\mathbf{x}_2) \frac{1}{r_{12}} \chi_j(\mathbf{x}_1) \tag{2.12}$$

$$\hat{K}_k(\mathbf{x}_1) \chi_j(\mathbf{x}_1) = \int \mathrm{d}\mathbf{x}_2 \chi_k^*(\mathbf{x}_2) \chi_j(\mathbf{x}_2) \frac{1}{r_{12}} \chi_j(\mathbf{x}_1). \tag{2.13}$$

$\hat{J}_k(\mathbf{x}_1)\chi_j(\mathbf{x}_1)$ has a simple classical interpretation. It is the repulsion energy between an electron occupying orbital χ_j and the charge density created by an electron occupying orbital χ_k. $\hat{J}_k$ is therefore called the Coulomb operator. $\hat{K}_k$ is called exchange operator. It does not have a classical interpretation, but reflects

the Pauli's principle. Since the orbital variations $\delta\chi_j$ are arbitrary and (2.11) holds for all variations, it follows that

$$\left\{\hat{h}_j + \sum_k^N \hat{J}_k - \hat{K}_k\right\}\chi_j = \sum_k^N \epsilon_{kj}\chi_k$$
$$\Rightarrow \hat{f}\chi_j = \sum_k^N \epsilon_{kj}\chi_k, \tag{2.14}$$

where the Fock operator $\hat{f}$ is defined. It should be noted that the above equation is invariant under unitary transformations of the orbitals. It can be transformed into the form [5]

$$\hat{f}\chi_j = \epsilon_j\chi_j. \tag{2.15}$$

These are the canonical Hartree-Fock equations, often simply called Hartree-Fock equations. The two important aspects of this approach are, that (a) the wave function is represented only by a single Slater determinant and (b) the electrons occupying the orbitals interact only with the mean field created by the charge density of the other electrons. As a result of these approximations electron-electron correlation is neglected.

The Hartree-Fock equations are formulated in terms of the spin orbitals. For purposes described in the next section, it is useful to reformulate them in terms of the spatial orbitals. Each spin orbital is given by a product of a spatial orbital and a spin function. There are two spin functions corresponding to spin up and spin down,

$$\chi_j(\mathbf{x}) = \psi_j(\mathbf{r})\sigma_j(\omega) = \begin{cases} \psi_j(\mathbf{r})\alpha(\omega) \text{ or,} \\ \psi_j(\mathbf{r})\beta(\omega) \end{cases}. \tag{2.16}$$

The spin functions are taken to be orthonormal. Since the electronic Hamiltonian (2.2) is independent of the spin, it should be possible to simply integrate the spin variable out. However, in Hartree-Fock theory the spin has to be taken into

account because the Fock operator indirectly depends on the spin. This can be seen from (2.13) by noting that

$$\begin{aligned}\hat{K}_k(\mathbf{x}_1)\chi_j(\mathbf{x}_1) &= \int \mathrm{d}\mathbf{x}_2 \chi_k^*(\mathbf{x}_2)\chi_j(\mathbf{x}_2)\frac{1}{r_{12}}\chi_j(\mathbf{x}_1) \\ &= \int \mathrm{d}\mathbf{r}_2 \mathrm{d}\omega_2 \psi_k^*(\mathbf{r}_2)\psi_j(\mathbf{r}_2)\sigma_k^*(\omega_2)\sigma_j(\omega_2)\frac{1}{r_{12}}\chi_k(\mathbf{x}_1) \\ &= \delta_{\sigma_k\sigma_j}\int \mathrm{d}\mathbf{r}_2 \psi_k^*(\mathbf{r}_2)\psi_j(\mathbf{r}_2)\frac{1}{r_{12}}\chi_k(\mathbf{x}_1). \end{aligned} \tag{2.17}$$

For the sake of simplicity, it is assumed that all spatial orbitals are doubly occupied. The Hartree-Fock equations then take the form of the restricted Hartee-Fock equations

$$\hat{f}\psi_j = \left\{\hat{h}_j + \sum_k^{N/2} 2\hat{J}_k - \hat{K}_k\right\}\psi_j = \epsilon_j\psi_j. \tag{2.18}$$

2.2 Roothaan-Hall equations

In this section, it is shown how to solve the restricted Hartree-Fock equations numerically. To this aim, the spatial orbitals are expanded in a finite set of basis function $\{\phi_j(\mathbf{r})\}_{j=1\cdots K}$

$$\psi_j = \sum_{k=1}^{K} C_{kj}\phi_k. \tag{2.19}$$

Within the space spanned by the basis set, a wave function represented by a single Slater determinant is completely determined by the coefficient matrix $\mathbf{C}$. Using the basis set expansion in (2.18) yields

$$\begin{aligned} &\hat{f}\sum_k^K C_{kj}\phi_k = \epsilon_j \sum_{k=1}^K C_{kj}\phi_k \\ \Rightarrow &\sum_k^K C_{kj}\int \mathrm{d}\mathbf{r}\phi_l^*(\mathbf{r})\hat{f}\phi_k(\mathbf{r}) = \epsilon_j \sum_k^K C_{kj}\int \mathrm{d}\mathbf{r}\phi_l^*(\mathbf{r})\phi_j(\mathbf{r}) \\ \Rightarrow &\sum_k^K C_{kj}F_{lk} = \epsilon_j C_{kj}S_{lk} \\ \Rightarrow &\mathbf{FC} = \mathbf{SC}\epsilon. \end{aligned} \tag{2.20}$$

It is important to note that the Roothan-Hall equation is not a generalized eigenvalue problem since the Fock matrix **F** depends on the coefficient **C**. Thus it has to be solved iteratively. If the basis set used is orthonormal, the overlap matrix **S** reduces to the identity matrix. With the two electron integrals

$$(jk|mn) = \int \mathrm{d}\mathbf{r}_1 \mathrm{d}\mathbf{r}_2 \phi_j^*(\mathbf{r}_1)\phi_k(\mathbf{r}_1)\frac{1}{r_{12}}\phi_m^*(\mathbf{r}_2)\phi_n(\mathbf{r}_2) \tag{2.21}$$

it is possible to express the relevant operators in terms of the basis function. The representation of the one particle part of the Fock operator is given by

$$H_{jk}^{core} = -\int \mathrm{d}\mathbf{r}_1 \phi_j^*(\mathbf{r}_1)\frac{1}{2}\Delta\phi_k(\mathbf{r}_1) + \int \mathrm{d}\mathbf{r}_1 \sum_A \phi_j^*(\mathbf{r}_1)\frac{Z_A}{r_{1A}}\phi_k(\mathbf{r}_1). \tag{2.22}$$

The Coulomb operator is represented as

$$\begin{aligned}\left(\hat{J}_j\right)_{kl} &= \int \mathrm{d}\mathbf{r}_1 \phi_k^*(\mathbf{r}_1)\hat{J}_j\phi_l(\mathbf{r}_1) \\ &= \sum_m^K \sum_n^K \int \mathrm{d}\mathbf{r}_1 \mathrm{d}\mathbf{r}_2 \phi_k^*(\mathbf{r}_1) C_{mj}^* \phi_m^*(\mathbf{r}_2)\frac{1}{r_{12}} C_{nj}\phi_n(\mathbf{r}_2)\phi_l(\mathbf{r}_1) \\ &= \sum_m^K \sum_n^K C_{mj}^* C_{nj}(kl|mn)\end{aligned} \tag{2.23}$$

and similarly the exchange operator

$$\left(\hat{K}_j\right)_{kl} = \sum_m^K \sum_n^K C_{mj}^* C_{nj}(kn|ml). \tag{2.24}$$

Thus for the restricted Hartree-Fock case

$$\begin{aligned}F_{jk} &= H_{jk}^{core} + \sum_a^{N/2} \sum_m^K \sum_n^K C_{ma}^* C_{na} \left\{2(jk|mn) - (jn|mk)\right\} \\ &= H_{jk}^{core} + \sum_m^K \sum_n^K P_{nm} \left\{(jk|mn) - \frac{1}{2}(jn|mk)\right\}\end{aligned} \tag{2.25}$$

holds. Where the density matrix **P** is defined as

$$P_{jk} = 2\sum_a^{N/2} C_{ja} C_{ka}^*. \tag{2.26}$$

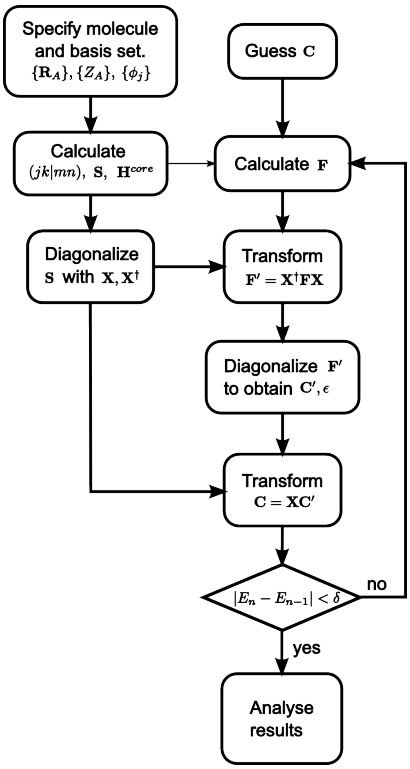

Figure 2.1: Schematic view of a SCF procedure

Like the coefficient matrix $\mathbf{C}$, the density matrix $\mathbf{P}$ completely specifies the wave function within the space spanned by the basis.

A solution of (2.20) is usually called the self-consistent field. A simple algorithm to solve (2.20) is scetched in figure 2.1. To start the iteration, one needs a guess of the coefficients. $\mathbf{H}^{core}$ only needs to be calculated once, but the two electron part of the Fock matrix has to be reassembled during every iteration. The energy difference of two subsequent iterations usually serves as a convergence criterion. A way to analyse the results of a SCF calculation is the Mulliken population analysis. Since

$$\begin{aligned} N &= 2\sum_a^{N/2} \int \mathrm{d}\mathbf{r} |\psi_a(\mathbf{r})|^2 = \sum_j^K \sum_k^K P_{kj} S_{jk} = \sum_j^K \mathrm{tr}(\mathbf{PS})_{jj} \\ &= \mathrm{tr}(\mathbf{PS}) \end{aligned} \tag{2.27}$$

holds, $\mathrm{tr}(\mathbf{PS})_{jj}$ can be interpreted as the charge occupying the basis function ϕ_j. However, this interpretation is not unique because the trace is cyclic, i.e.

$$\mathrm{tr}(\mathbf{PS}) = \mathrm{tr}(\mathbf{PS}^\alpha \mathbf{S}^{1-\alpha}) = \mathrm{tr}(\mathbf{S}^{1-\alpha}\mathbf{PS}^\alpha) = N. \tag{2.28}$$

The Mulliken population analysis corresponds to the choice $\alpha = 0$. Another often used possibility is the Löwdin population analysis with $\alpha = 1/2$.

With similar considerations as above - and taking into account the spin dependence of the exchange operator - it is possible to derive the basis set representation of the unrestricted Hartree-Fock equation. This yields two sets of equations, one for each spin

$$\begin{aligned}\mathbf{F}^{\alpha}\mathbf{C}^{\alpha} =& \mathbf{S}\mathbf{C}^{\alpha}\epsilon^{\alpha} \\ F_{jk}^{\alpha} =& H_{jk}^{core} + \sum_{a}^{N^{\alpha}}\sum_{m}^{K}\sum_{n}^{K}\left(C_{ma}^{\alpha}\right)^{*} C_{na}^{\alpha}\left\{(jk|mn) - (jn|mk)\right\} + \\ & \sum_{a}^{N^{\beta}}\sum_{m}^{K}\sum_{n}^{K}\left(C_{ma}^{\beta}\right)^{*} C_{na}^{\beta}(jk|mn)\end{aligned} \tag{2.29}$$

and vice versa.

2.3 Time-dependent Hartree-Fock equations

Knowing the exact solutions of (2.2), i.e. knowing the complete set of eigenfunctions of the electronic Hamiltonian, implies the knowledge of the time evolution of a system subject to the Hamiltonian (2.2) since the time evolution of an eigenfunction $\Psi_n(t)$ is given by

$$\Psi_n(t) = \exp\left\{-iE_n t\right\}\Psi(0), \tag{2.30}$$

where E_n is the corresponding eigenvalue. As pointed out before, it is in general not possible to obtain the analytic eigenfunctions of the Hamiltonian. Therefore, a similar strategy, as for the stationary case, is deployed to find approximative solutions of the time-dependent Schrödinger equation. Again the wave function is represented by a single Slater determinante

$$\Psi(t, \chi_1, \chi_2, \cdots, \chi_N) = \frac{1}{\sqrt{N!}}\sum_{\sigma\in S_N}\mathrm{sgn}(\sigma)\prod_{j=1}^{N}\chi_{\sigma(j)}(t, \mathbf{x}_j), \tag{2.31}$$

composed from time-dependent orbitals. Then Dirac-Frenkel variational principle [6] is used to derive the time-dependent Hartree-Fock equations. The action

$$S = \int_{t_0}^{t_1}\mathrm{d}t\langle\Psi(t)|\hat{H} - i\partial_t|\Psi(t)\rangle \tag{2.32}$$

is minimized with respect to the orbital variations, that fulfill

$$\langle \delta\chi_j | \chi_k \rangle = \int \mathrm{d}\mathbf{x} \delta\chi_j^*(\mathbf{x})\chi_k(\mathbf{x}) = 0. \tag{2.33}$$

It can be written as [7]

$$\langle \delta\Psi | L | \Psi \rangle = \langle \delta\Psi | \hat{H} - i\partial_t | \Psi \rangle = 0. \tag{2.34}$$

With this equation (2.34) can written as

$$\begin{aligned}
\langle \delta\Psi | \hat{H} - i\partial_t | \Psi \rangle =& \sum_{j=1}^{N} \langle \delta\chi_j^* | \hat{h}_j | \chi_j \rangle - i\langle \delta\chi_j^* | \partial_t | \chi_j \rangle + \\
& \sum_{j,k}^{N} \langle \delta\chi_j\chi_k | \frac{1}{r_{12}} | \chi_j\chi_k \rangle + \langle \chi_j\delta\chi_k | \frac{1}{r_{12}} | \chi_j\chi_k \rangle - \\
& \langle \delta\chi_j\chi_k | \frac{1}{r_{12}} | \chi_k\chi_j \rangle - \langle \chi_j\delta\chi_k | \frac{1}{r_{12}} | \chi_k\chi_j \rangle \\
=& \sum_{j}^{N} \int \mathrm{d}\mathbf{x}_1 \delta\chi_j^* \left\{ \hat{h}_j(\mathbf{x}_1) + \sum_{k=1}^{N} \hat{J}_k(\mathbf{x}_1) - \hat{K}_k(\mathbf{x}_1) - i\partial_t \right\} \chi_j(\mathbf{x}_1) \\
=& 0 \\
\Rightarrow i\partial_t\chi_j =& \hat{f}\chi_j.
\end{aligned} \tag{2.35}$$

The derivation of the relations

$$\langle \delta\Psi | \partial_t | \Psi \rangle = \sum_{j}^{N} \langle \delta\chi_j | \partial_t | \chi_j \rangle, \tag{2.36}$$

$$\langle \delta\Psi | \sum_{j}^{N} \hat{h}_j | \Psi \rangle = \sum_{j}^{N} \langle \delta\chi_j | \hat{h}_j | \chi_j \rangle \tag{2.37}$$

and

$$\begin{aligned}
\langle \delta\Psi | \frac{1}{r_{jk}} | \Psi \rangle =& \langle \delta\chi_j\chi_k | \frac{1}{r_{12}} | \chi_j\chi_k \rangle + \langle \chi_j\delta\chi_k | \frac{1}{r_{12}} | \chi_j\chi_k \rangle - \\
& \langle \delta\chi_j\chi_k | \frac{1}{r_{12}} | \chi_k\chi_j \rangle - \langle \chi_j\delta\chi_k | \frac{1}{r_{12}} | \chi_k\chi_j \rangle
\end{aligned} \tag{2.38}$$

is shown in A.1.

It was pointed out in the literature [8] that the Dirac-Frenkel variational principle

is flawed since it does not always lead to a minimum of the action. To ensure a true minimum it is proposed to use

$$\mathrm{Im}\langle\delta\Psi|\hat{H} - i\partial_t|\Psi\rangle = 0 \tag{2.39}$$

instead [7]. However, in the case of the time-dependent Hartree-Fock equations it yields the correct minimum. But a correction to the total wavefunction is needed

$$\Psi'(t) = \exp\left\{i\int_0^t \mathrm{d}t'\langle G(t')\rangle\right\}\Psi(t), \tag{2.40}$$

where $\Psi(t)$ is a single Slater determinant formed from a set of orbitals which are evolving in time due to (A.1), and $G(t)$ is the electron electron repulsion energy. Since the problem is non-linear, i.e., the Fock operator depends on the orbitals, the solution of the (stationary) Hartree-Fock equations does not solve the time-dependent Hartree-Fock equations, as would be the case for the full electronic Schrödinger equation (2.2). The formal solution of (2.35) is given by the time evolution operator

$$\chi_j(t) = \hat{T}\exp\left\{-i\int_0^t \mathrm{d}t'\hat{f}(t')\right\}\chi_j(0). \tag{2.41}$$

Due to the time-ordering operator $\hat{T}$, this expression cannot in general be evaluated analytically. Again one has to rely one numerical solutions.

2.4 Summary

In this chapter, we presented a derivation of both the stationary and time-dependent Hartree-Fock equations. The derivations followed the original approaches of Hartree and Dirac. This sets the theoretical framework in which the work was done. An important concern in quantum chemical calculations is the choice or construction of a proper basis set. Since the construction of new basis sets is beyond the scope of this thesis, gaussian basis sets commonly used in quantum chemical calculations are used.

3

Numerical solution of the time-dependent Hartree-Fock equations

To solve the time-dependent Hartree-Fock equation numerically, approximations to (2.41) are used. In order to select a method suitable for large molecules, the Euler, the second order differencing and the time evolution operator scheme are described. They are are tested for both a one-dimensional and more realistic atomic and molecular systems.

For the algorithms presented below, it is assumed that the Fock operator $\hat{f}$ stays constant over a small time interval Δt. Equation (2.41) then reduces to

$$\chi_j(t + \Delta t) = \exp\left\{-i\Delta t \hat{f}(t)\right\} \chi_j(t). \tag{3.1}$$

For the sake of brevity, the algorithms below are described only for the closed shell case. This case is then extended to open shell systems by two coupled equations, one for each spin with the according Fock operators.

To test the stability of the different integrators, the ground states of the test systems are propagated in time and the conservation of the norm $|\langle\Psi(t)|\Psi(t)\rangle|$ and the energy $E(t) = \langle\Psi(t)|\hat{H}|\Psi(t)\rangle$ of the wave function are monitored. Since the molecular orbitals that compose the ground state are approximative eigenvectors

of the Fock matrix the time propagation should only yield an oscillating phase factor, i.e. the norm and the total energy should be conserved.

The electronic processes under consideration, i.e. the Auger effect, take place on a time scale of a few femtoseconds. Thus, the integrator should at least be stable on this time scale.

First the systems used for testing the integration schemes are briefly introduced. Then the different integration schemes are discussed. In the end the performance of the second order differencing and the time evolution operator scheme are tested.

3.1 Quantum harmonic oscillator

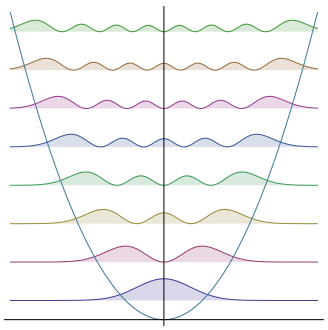

Figure 3.1: The first eigenfunctions of the quantum harmonic oscillator

The quantum harmonic oscillator serves as a simple, one-dimensional model system. To include electronic interaction, not one but a few particles are confined by the harmonic potential. The particles repel each other with the potential

$$V_{pp} = \frac{\operatorname{erf}(r)}{r}. \tag{3.2}$$

This mimics the Coulomb interaction among the electrons. The Coulomb potential $1/r$ cannot be used in one dimension, because the two electron integrals (2.21) would diverge. Thus the interaction among the particles is scaled down in this model (3.2). A SCF program was implemented to solve the Roothaan-Hall equations for this system. The eigenfunctions of the one particle harmonic oscillator

$$\phi_n(r) = \sqrt{\frac{1}{2^n n! \sqrt{\pi}}} \exp\left\{-\frac{1}{2}r^2\right\} H_n(r) \tag{3.3}$$

are used as basis functions. The implementation is described in A.2.

For both the stability tests and the application the first 10 basis functions, ϕ_0 to

ϕ_9, are used. The basis function ϕ_9 has an energy value of $E_9 = 9.5\,\mathrm{H}$. During the time propagation this corresponds to an oscillation with a period of $T \approx 0.66\,\hbar/\mathrm{H}$. To sample this oscillation properly, the integration time step should not be larger than $\Delta t = 0.01\,\hbar/\mathrm{H} \approx 0.24\,\mathrm{as}$ according to the Nyquist sampling theorem. This holds independently of the integration scheme used.

3.2 Carbon

The carbon atom with the basis sets STO-3G [9] and 6-31G [10] is used as a simple three-dimensional test system. The STO-3G basis contains five basis functions (two s-type and one set of p-type functions) and can be considered a small basis set. The 6-31G is a medium sized basis set. It contains 9 basis functions (three s-type and two sets of p-type basis functions). The electronic ground state is calculated with the quantum chemistry program `Gaussian 03` [11] with Hartree-Fock theory. The convergence criterion for the SCF procedure was set to $\Delta E = 10^{-6}\,\mathrm{H}$

The basis function with the fastest oscillating coefficient is for both basis sets the $1s$-function. In both cases it has an energy value of about $-18H$. This relates to a period of about $0.34\,\hbar/\mathrm{H} \approx 8.4\,\mathrm{as}$. Thus, a step size of $\Delta t = 0.01\,\hbar/\mathrm{H} \approx 0.24\,\mathrm{as}$ is sufficient.

3.3 Alkanes

For more systematic stability tests, the first five alkanes (methane (CH_4), ethane (C_2H_6), propane (C_3H_8), butane (C_4H_{10}) and pentane (C_5H_{12})) are used. The basis sets STO-3G, 6-31G and cc-pVDZ [12] are employed. The latter one is a large basis set containing five basis functions for hydrogen (two s-type and one set of p-type functions) and 14 basis functions for carbon (three s-type, two sets of p-type and one set of d-type functions). Also for the cc-pVDZ basis set an

integration time step of about 0.24 as is sufficient.

Figure 3.2 shows the structure and the electron density of the ground state

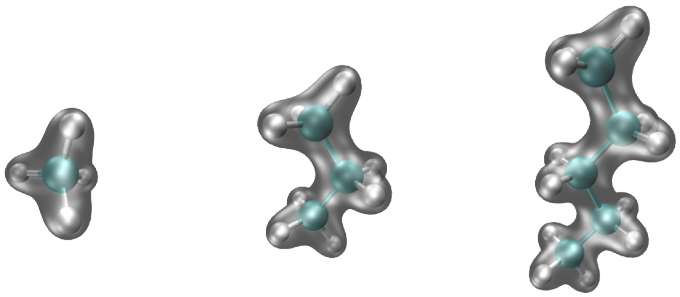

Figure 3.2: Structure and ground state electron density of methane, propane and pentane for the cc-pVDZ basis set

methane, propane and pentane. The structure was optimized with `Gaussian 03`. The convergence tresholds for the structure optimization were $3 \cdot 10^{-4} \frac{\mathrm{H}}{a_0}$ for the RMS force and $1.2 \cdot 10^{-3} a_0$ for the RMS displacement.

3.4 Euler scheme

To derive the Euler scheme, the exponential in (3.1) is expanded to the first order,

$$\exp\left\{-i\Delta t\hat{f}\right\} = 1 - i\Delta\hat{f} + O(\Delta t)^2 \tag{3.4}$$

and equation (3.1) yields

$$\chi_j(t+\Delta t) = \chi_j(t) - i\Delta\hat{f}(t)\chi_j(t) + O(\Delta t)^2. \tag{3.5}$$

The Euler scheme is therefore a first order scheme. Using the basis set expansion (2.19), one obtains

$$\begin{aligned} &\mathbf{SC}(t+\Delta t) = \mathbf{SC}(t) - i\Delta t\mathbf{F}(t)\mathbf{C}(t) \\ \Rightarrow\ &\mathbf{C}(t+\Delta t) = \mathbf{C}(t) - i\Delta t\mathbf{S}^{-1}\mathbf{F}(t)\mathbf{C}(t). \end{aligned} \tag{3.6}$$

The overlap matrix $\mathbf{S}$ can be inverted since $\mathbf{S}$ is hermitian. Figure 3.3 shows a flow chart of the algorithm. Since the basis functions do not change in time, the overlap matrix $\mathbf{S}$, the representation of the core Hamiltonian $\mathbf{H}^{core}$ and the two electron integrals $(jk|mn)$ only need to be calculated at the beginning. For the quantum harmonic oscillator this is done with the SCF program described in 3.1. For the atoms and molecules the quantum chemistry program `Gaussian 03` is used. The overlap matrix $\mathbf{S}$ is then inverted using Intel's `Math Kernel Library`. In every integration step the Fock matrix $\mathbf{F}(t)$ is assembled using the current coefficient matrix $\mathbf{C}(t)$. The Fock matrix is then used to propagate the coefficients $\mathbf{C}(t)$ to obtain the next coefficients $\mathbf{C}(t+\Delta t)$.

Instead of explicitly inverting the overlap matrix $\mathbf{S}$ and performing the matrix multiplication $\mathbf{S}^{-1}\mathbf{F}$, it would numerically be more stable to directly calculate $\mathbf{S}^{-1}\mathbf{F}$ by Gauss elimination.

3.4.1 Quantum harmonic oscillator

First the Euler scheme is tested with a two and a four particle ground state of the quantum harmonic oscillator 3.1. The largest possible integration time

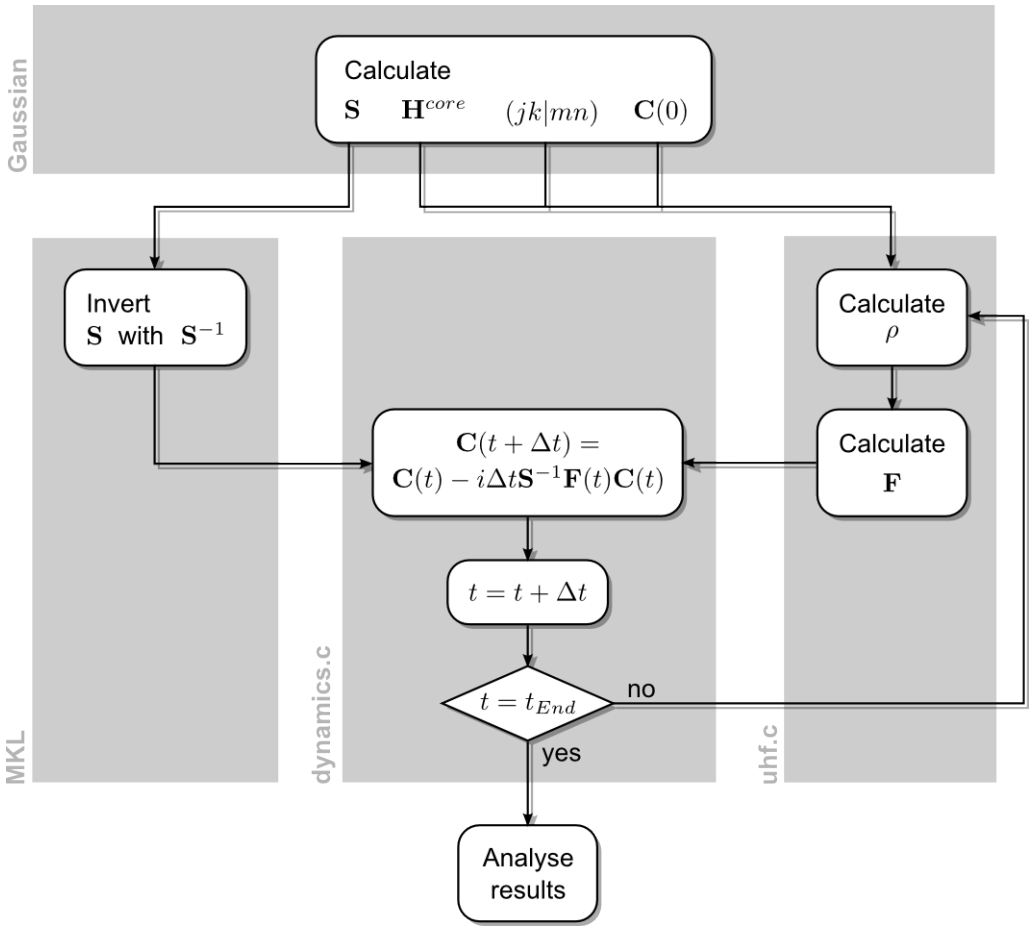

Figure 3.3: Flow chart of the Euler scheme

step for the quantum harmonic oscillator with the first 10 basis functions is $\Delta t = 0.01\,\hbar/\mathrm{H} \approx 0.24\,\mathrm{as}$. To test the effect of the integration time step, the integration time step of $\Delta t = 0.001\,\hbar/\mathrm{H} \approx 0.024\,\mathrm{as}$ is additionally considered.

Figure 3.4 shows the time evolution of the total energy and the norm of the two particle ground state. For the larger time step the energy and the norm have increased by more then 20% after about 200 as. For the smaller time step the increase of the norm and energy is slower. After 1 fs the norm and the energy have increased by about 10%. Figure 3.5 shows the time evolution of the total energy and the norm of the four particle ground state. The increase of the total energy and the norm is faster than in the two particle system. Even for the

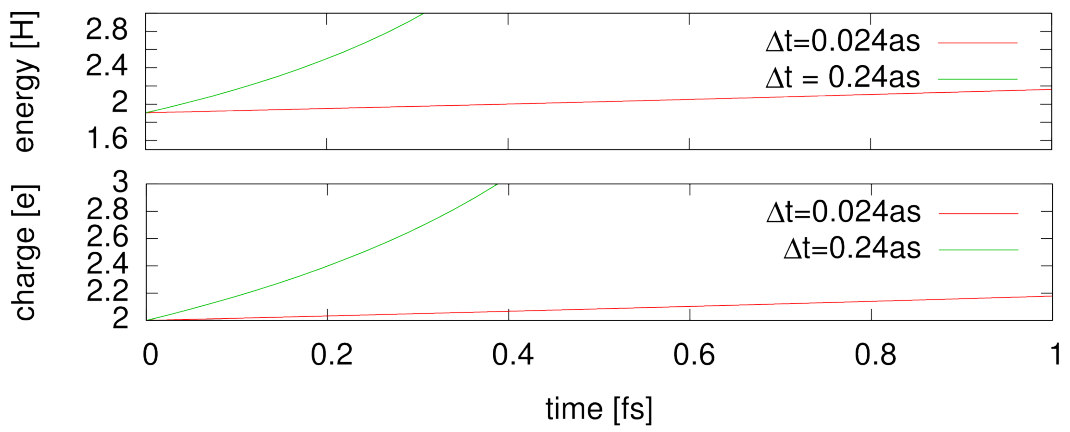

Figure 3.4: Time evolution of the total energy (top) and the norm (bottom) of the two particle ground state

smaller time step $\Delta t = 0.001\hbar/\mathrm{H}$ the energy and the norm have increased by almost 10% after 200 as.

For both systems the drift of the total energy and the norm is about ten times slower for the ten times smaller time step. This is typical for a first order scheme and a well known problem of the Euler scheme [13]. Thus the energy and norm drift is caused by the discretization error. The Euler scheme is not further tested because it is unstable for the systems shown above.

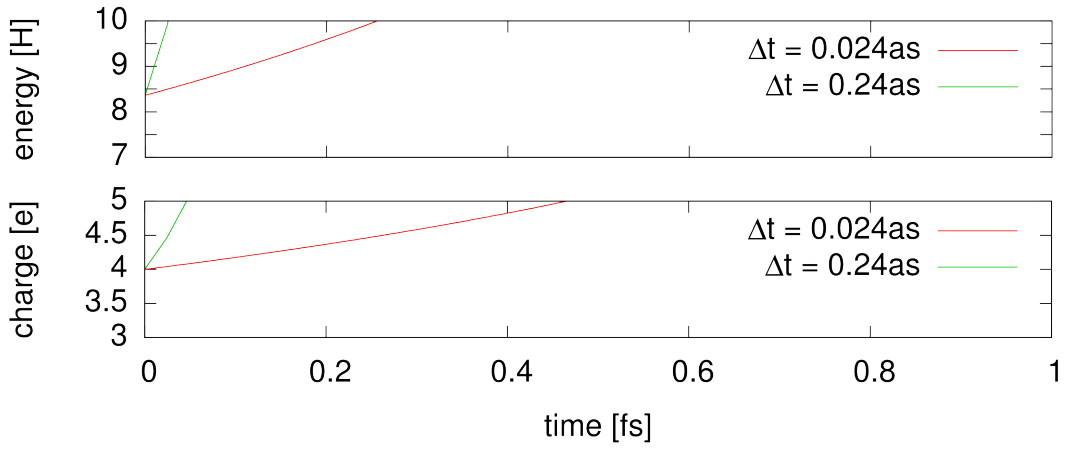

Figure 3.5: Time evolution of the total energy (top) and the norm (bottom) of the four particle ground state

3.5 Second-order differencing

To overcome the instability of the Euler scheme, the discretization error has to be reduced. To this aim, a two step scheme is used. To derive the second-order differencing scheme [14], a forward and backward propagation of equation (3.1) is used

$$\begin{aligned}\chi_j(t+\Delta t) - \chi_j(t-\Delta t) &= \left(\exp\left\{-i\Delta t\hat{f}\right\} - \exp\left\{i\Delta t\hat{f}\right\}\right)\chi_j(t) \\ \Rightarrow \chi_j(t+\Delta t) &= \chi_j(t-\Delta t) - 2i\Delta t\hat{f}\chi_j(t) + O(\Delta t)^3 \\ \Rightarrow \mathbf{C}(t+\Delta t) &= \mathbf{C}(t-\Delta t) - 2i\Delta t\mathbf{S}^{-1}\mathbf{F}(t)\mathbf{C}(t) + O(\Delta t)^3. \quad (3.7)\end{aligned}$$

In this scheme the quadratic terms in Δt cancel out. Accordingly, this integration scheme is correct to the second order in the time step Δt. A single integration step with the Euler scheme is used to start off the integration with the second-order differencing scheme.

In figure 3.6 the implementation of the second-order differencing scheme is sketched. The main difference to the implementation of the Euler scheme is that an additional $K \times K$ matrix for $\mathbf{C}(t-\Delta t)$ has to be stored. The additional memory consumption is negligible compared to the storage of the two electron integrals (2.21).

The expenditure of time is also higher than in the Euler scheme due to the bookkeeping of the additional matrix. However, the expense for the bookkeeping scales as $O(K^2)$ and is, therefore, negligible compared to the matrix multiplication and the assembly of the Fock matrix.

Thus, the second-order differencing provides a smaller discretization error than the Euler scheme for little extra computational expenses.

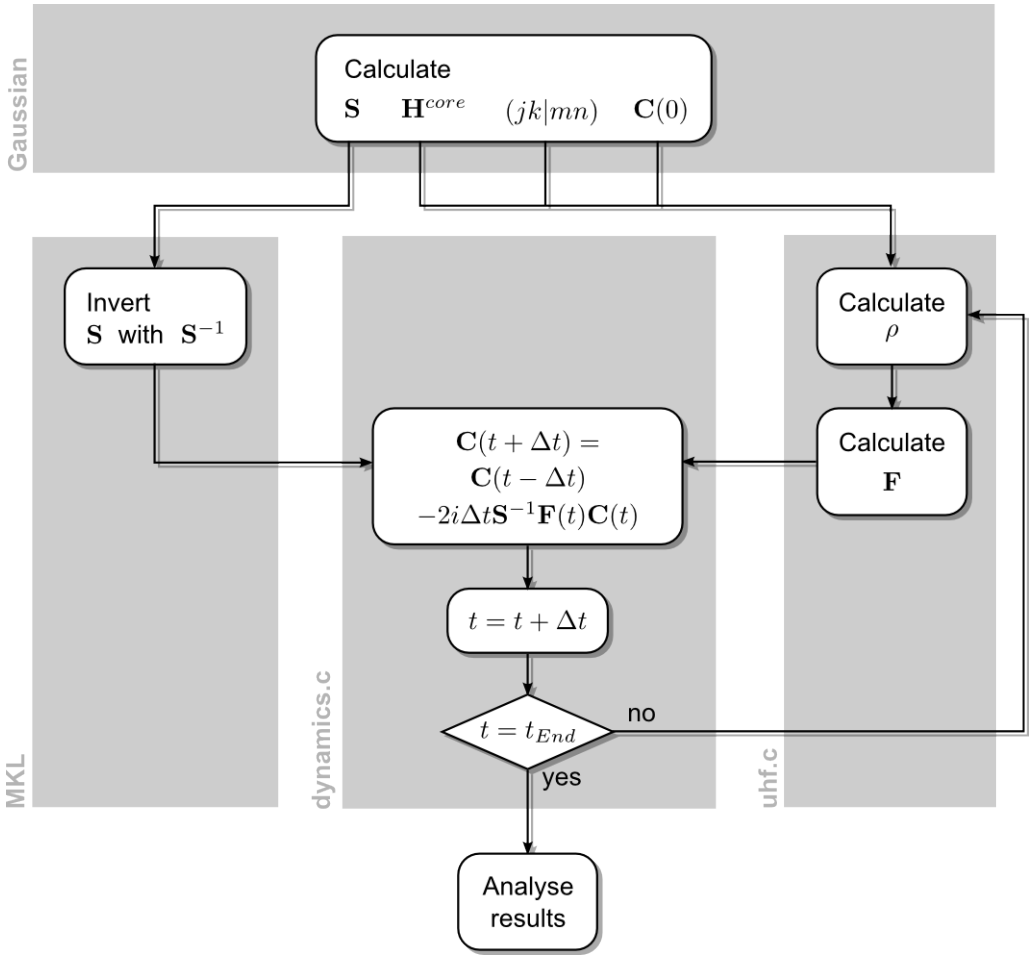

Figure 3.6: Implementation of the second-order differencing scheme

3.5.1 Harmonic oscillator

Figure 3.7 shows the propagation of an eight particle ground state of the harmonic oscillator defined in 3.1. For convenience the scaling of the two plots is chosen differently. As can be seen, for the larger time step (green) the energy and the

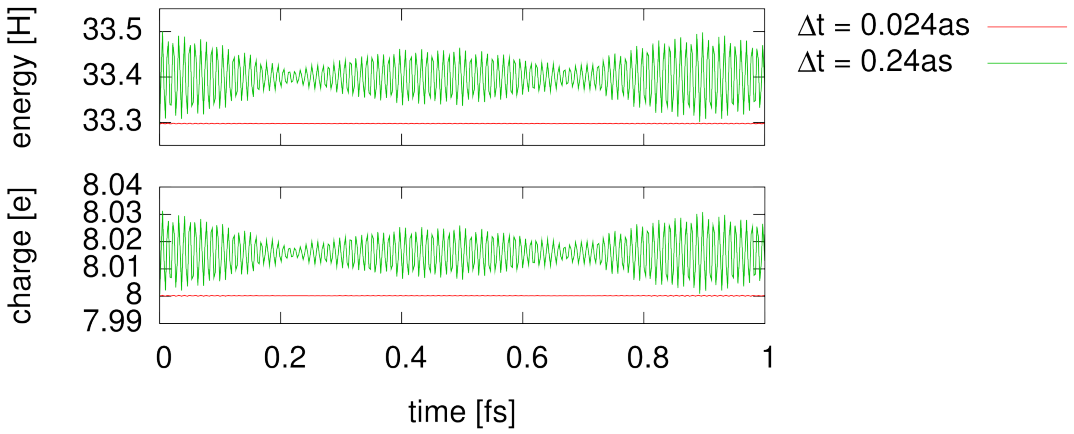

Figure 3.7: Time evolution of the total energy (top) and the norm (bottom) of the eight particle ground state

norm around oscillate. Also for the smaller time step (red) the norm and energy oscillate. However, this cannot be seen due to the scaling of the plot.

To get an quantitative overview of the oscillation, the amplitude of the oscillation of the energy for different step and system sizes is shown in figure 3.8. For the systems containing more particles, the oscillations are stronger due to the stronger interactions. For a step size of $\Delta t = 0.024\,\text{as}$ the amplitude of the oscillation is less $10^{-3}\,\text{H}$. This is less than one-tenth of a percent of the total energy of the smallest system.

There is also an energy drift during the integration. Figure 3.9 shows the differences of the running average after 10 fs and the initial value for different step and system sizes. The drift is faster for systems composed of more particles. This is also caused by the stronger interactions. Again the step size of $\Delta t = 0.024\,\text{as}$ yields good results. For this step size the energy drift is about $10^{-3}\,\text{H}$ after 10 fs

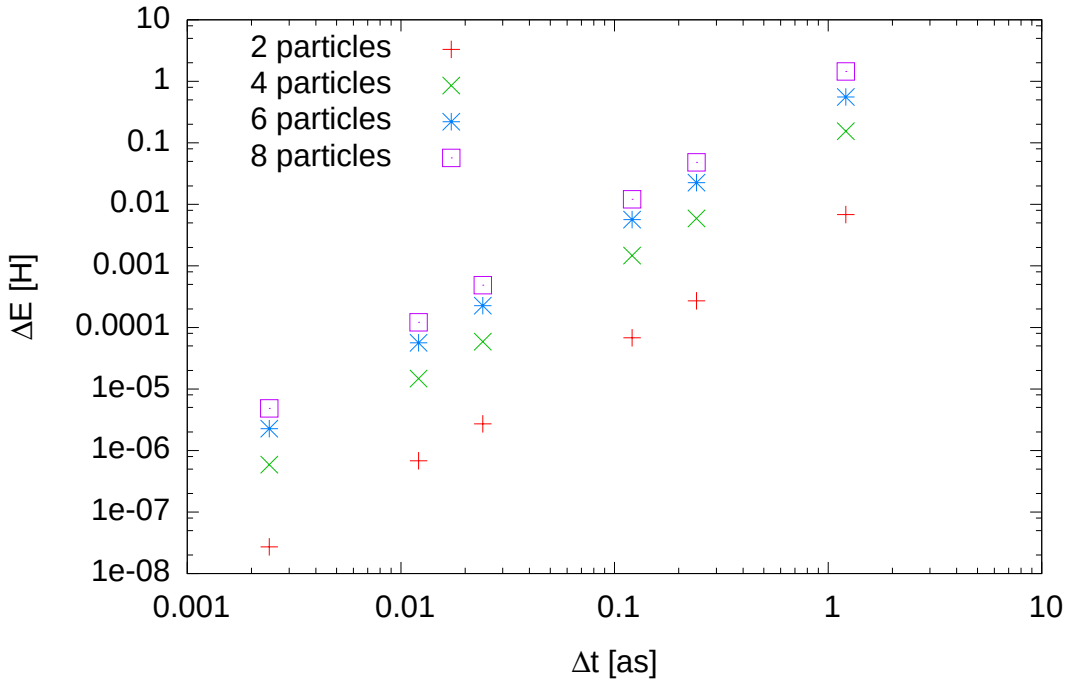

Figure 3.8: Amplitude of the oscillation averaged over 10 fs as a function of the step size Δt for the two, four, six and eight particle ground state

of integration.

In both plots the slope of the dependence of the step size is about 2. Since these are logarithmic plots, both the amplitude of the oscillation and the energy drift depend quadratically on the step size Δt. Thus, the second-order differencing is indeed a second order integration scheme.

The analysis above shows that the second-order differencing with a integration step of $\Delta t = 0.024$ as is long term stable for the quantum harmonic oscillator.

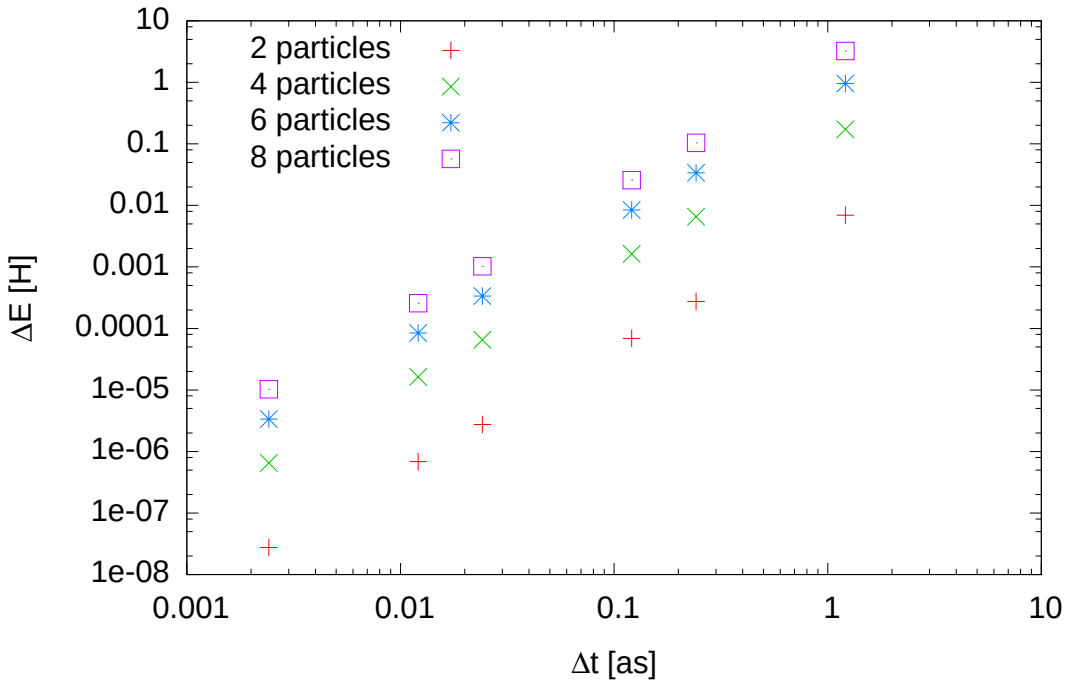

Figure 3.9: Difference between the running average of the energy and the inital value after 10 fs as a function of the step size for the two, four, six and eight particle ground state

3.5.2 Carbon

Since the second-order differencing is stable for the quantum harmonic oscillator, it is now tested with a real system. The carbon atom (see 3.2) is used with the STO-3G and 6-31G basis sets.

Figure 3.10 shows the time evolution of the total energy and the norm for the

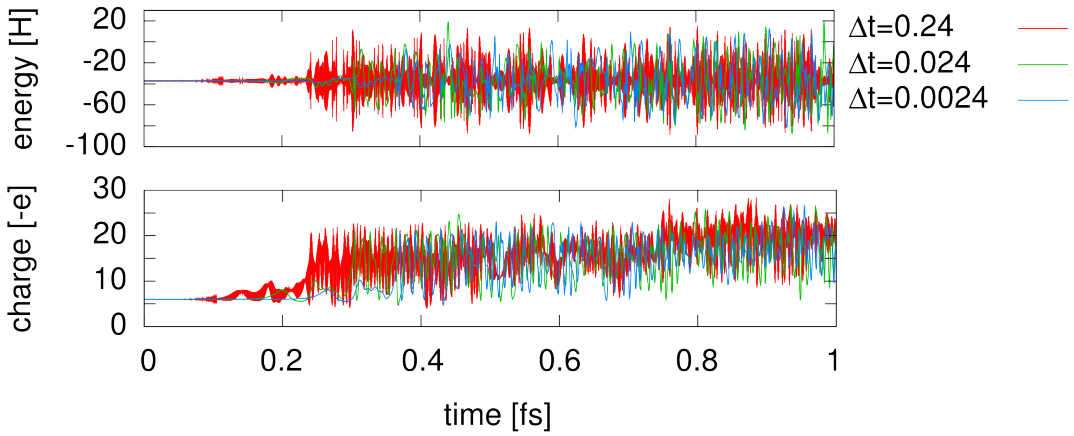

Figure 3.10: Time evolution of the total energy (top) and the norm (bottom) for different step sizes for the carbon ground state with the STO-3G basis set

three different time steps with the STO-3G basis set. Both the total energy and the norm oscillate which cannot be seen in the first 100 as due to the scaling. For the largest time step (red) the amplitude of oscillation of the energy increases strongly at about 200 as. At the same time the norm of the wave function increases strongly. A similar effect can be seen for the two shorter time steps, with a longer delay. After this sudden change the oscillations of the energy stay in the same range. The mean value of the oscillation of the norm drifts to higher values.

Figure 3.10 shows the time evolution of the total energy and the norm for three different time steps with the 6-31G basis set. A similar change in the time evolution of the energy and the norm as in the STO-3G basis set can be seen.
In both cases only the delay before the change depends on the time step. The

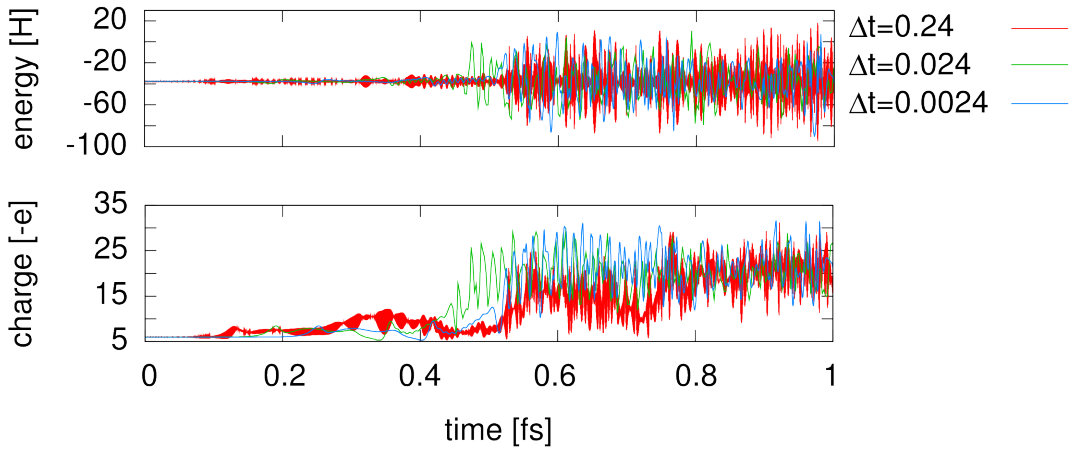

Figure 3.11: Time evolution of the total energy (top) and the norm (bottom) for different step sizes for the carbon ground state with the 6-31G basis set

amplitude of the oscillation and the drift of the norm is for all time steps the same. Thus, this instability is not caused by the discretization error.

3.6 Time evolution operator

The instability of the second-order differencing scheme for the carbon atom is not caused by the discretization error. Instead of using a higher than second order scheme, a different approach is used to overcome the instability.
From the definition of the Fock matrix (2.25) and (2.29), it is clear that both the restricted and the unrestricted Fock matrices are hermitian. Therefore, they can be diagonalised with an unitary matrix $\mathbf{U}$, so that

$$\mathbf{F} = \mathbf{U}^{\dagger}\mathbf{\Lambda}\mathbf{U}, \tag{3.8}$$

where $\mathbf{\Lambda}$ is diagonal with the eigenvalues of $\mathbf{F}$ as elements.
With the diagonalization of the Fock matrix it is possible to calculate the exponential in (3.1) directly. It is, therefore, not necessary to approximate the exponential.
For the derivation of the working equation consider an orthonormal basis set $\left\{\phi'_j\right\}$. Then

$$\begin{aligned}\langle\phi'_j|\exp\{\hat{f}\}|\phi'_k\rangle &= \langle\phi'_j|\sum_n \frac{1}{n!}\hat{f}^n|\phi'_k\rangle \\ &= \sum_n \frac{1}{n!}\sum_{i_1,i_2,\cdots i_{n-1}} \langle\phi'_j|\hat{f}|\phi'_{i_1}\rangle\langle\phi'_{i_1}|\hat{f}|\phi'_{i_2}\rangle\cdots\langle\phi_{i_{n-1}}|\hat{f}|\phi'_k\rangle \\ &= \sum_n \frac{1}{n!}\left(\mathbf{F}'^n\right)_{jk} = \exp\{\mathbf{F}\}\end{aligned} \tag{3.9}$$

holds, where the completeness relation

$$\sum_j |\phi'_j\rangle\langle\phi'_j| = \hat{1}. \tag{3.10}$$

has been used. Together with (3.1) this yields

$$\mathbf{C}'(t+\Delta t) = \exp\left\{-i\Delta t\mathbf{F}'(t)\right\}\mathbf{C}'(t). \tag{3.11}$$

Using the relation (3.8), equation (3.11) can be written as

$$\begin{aligned}\mathbf{C}'(t+\Delta t) &= \exp\left\{-i\Delta t\mathbf{U}'^{\dagger}(t)\mathbf{\Lambda}'(t)\mathbf{U}'\right\}\mathbf{C}'(t)\\ &= \sum_n \frac{(-i\Delta t)^n}{n!}\left(\mathbf{U}'^{\dagger}(t)\mathbf{\Lambda}'(t)\mathbf{U}'(t)\right)^n\mathbf{C}'(t)\\ &= \mathbf{U}'^{\dagger}(t)\sum_n \frac{(-i\Delta t)^n}{n!}\mathbf{\Lambda}'(t)^n\mathbf{U}'(t)\mathbf{C}'(t)\\ &= \mathbf{U}'^{\dagger}(t)\exp\left\{-i\Delta t\mathbf{\Lambda}'(t)\right\}\mathbf{U}'(t)\mathbf{C}'(t), \qquad (3.12)\end{aligned}$$

where $\mathbf{U}^{\dagger}\mathbf{U} = \mathbf{1}$ has been used.

The basis sets used in quantum chemistry are typically not orthonormal, but a given basis set $\{\phi_j\}$ can be orthonormalized to an orthonormal basis set $\{\phi'_j\}$ by a unitary transformation.

Figure 3.12 shows a flow chart of the time evolution operator scheme applied to non-orthonormal basis sets. Before the actual integration step, the coefficient matrix $\mathbf{C}(t)$ and the Fock matrix $\mathbf{F}(t)$ are transformed into an orthonormal basis set using the matrix $\mathbf{X}$. The transformed Fock matrix $\mathbf{F}'$ is then diagonalized and the time evolution operator is evaluated. The new coefficients $\mathbf{C}'(t\Delta t)$ is then transformed back into the original basis set. Using the coefficients $\mathbf{C}(t+\Delta t)$ the new Fock matrix assembled. The diagonalization of the overlap matrix $\mathbf{S}$, of the Fock matrix $\mathbf{F}$ and the inversion of the transformation matrix $\mathbf{X}$ are performed using routines provided by Intel's `MKL`.

Instead of performing the basis set transformation in every time step, it is possible to do the whole integration in the orthonormalized basis set. Therefor, the two electron integrals $(jk|mn)$ have to be transformed into the new basis too. However, this is scales as $O(K^5)$ and is, therefore, very expensive.

The basis set used for the quantum harmonic oscillator (3.1) is orthonormal. Accordingly, the transformation of the coefficients and the Fock matrix is not necessary.

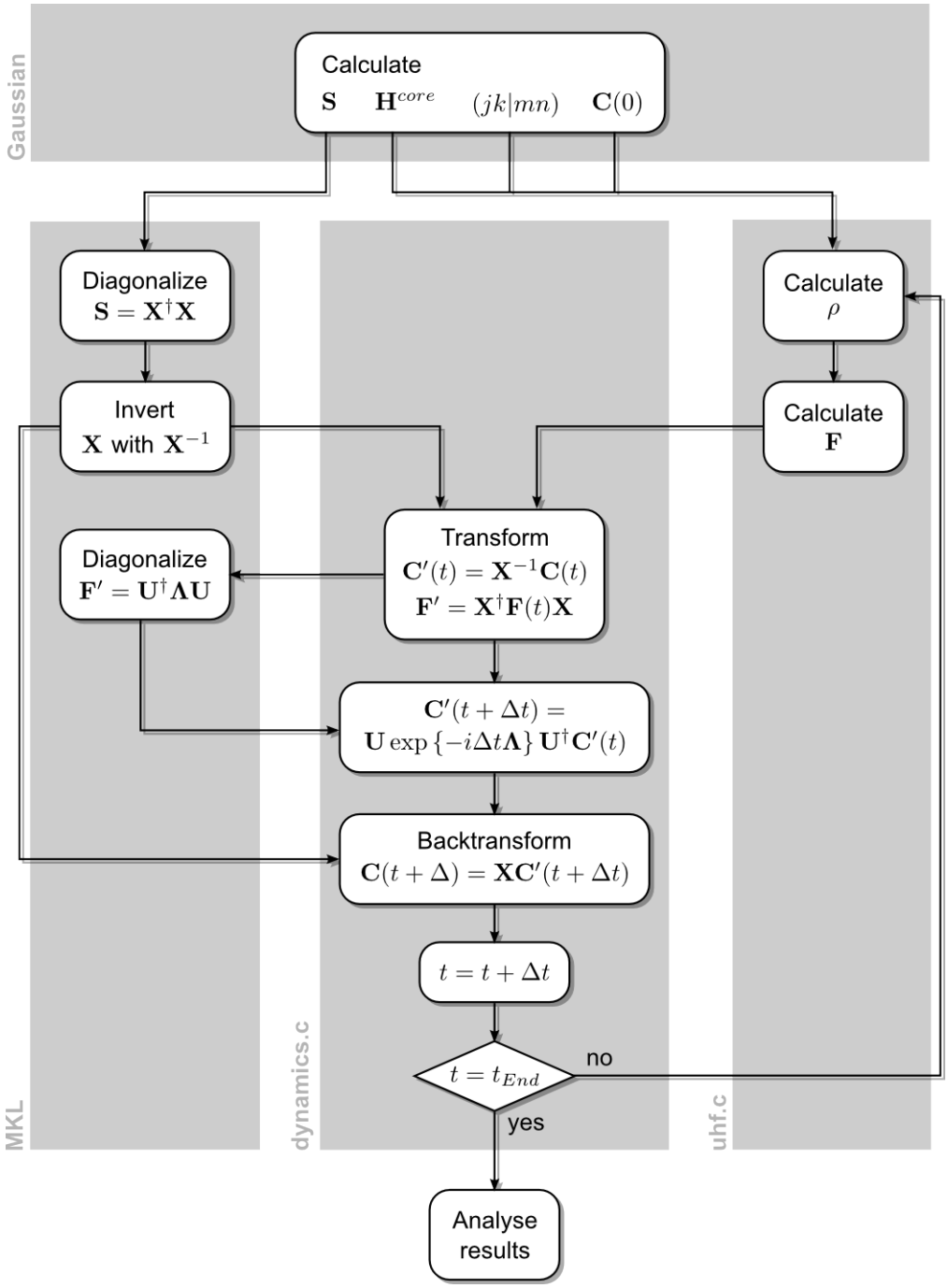

Figure 3.12: Flow chart of the time evolution operator scheme

3.6.1 Harmonic oscillator

Again an eight particle ground state is propagated in time. Figure 3.13 shows the time evolution of the total energy and the norm. For convenience not the absolute value, but the difference to the initial values $\Delta E = E(t) - E(0)$ and $|\langle\chi_j(0)|\chi_j(t)\rangle|$ are shown. The initial energy is about $E = 33.3\,\mathrm{H}$ and the initial norm is $8\,e$. As can be seen, the fluctuation of the norm is in a range of about $10^{-12}\,e$. In

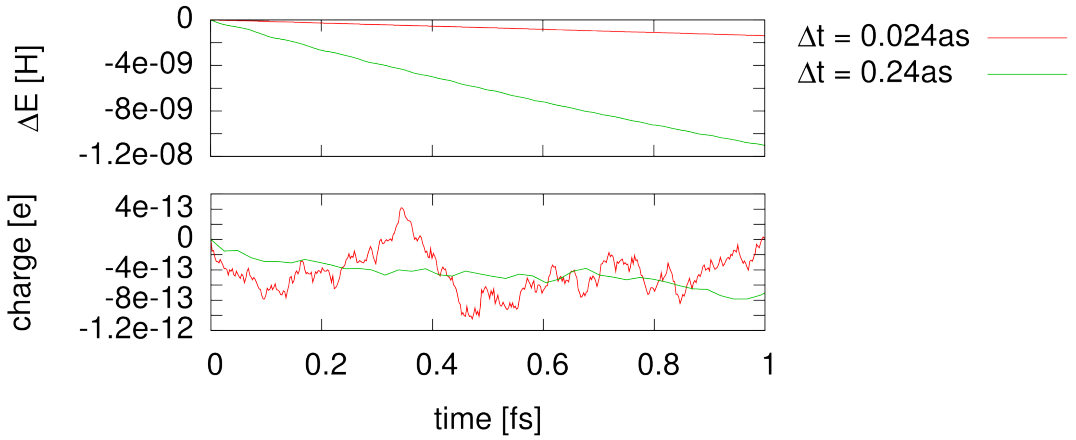

Figure 3.13: Time evolution of the total energy (top) and the norm (bottom) of the eight particle ground state for two different step sizes

this range the rounding errors caused by the limited numerical precision become important. This causes the larger fluctuations for the shorter time step (red). With the shorter time step more steps per time have to be performed. Thus, more rounding errors accumulate per time.

The energy drifts for both step sizes. The drift of the energy difference is about $\Delta E = 10^{-8}\,\mathrm{H}$ after 1 fs of integration time for the larger time step (green).

The norm is conserved within numerical precision. Thus the energy drift is tested more systematically. Figure (3.14 shows the energy drift after about 12 fs for different step and system sizes. In all cases the energy drift levels off for step sizes $\Delta t > 0.1\,\mathrm{as}$. However, step sizes $\Delta t > 0.1\,\mathrm{as}$ are not suitable due to insufficient sampling (see 3.1).

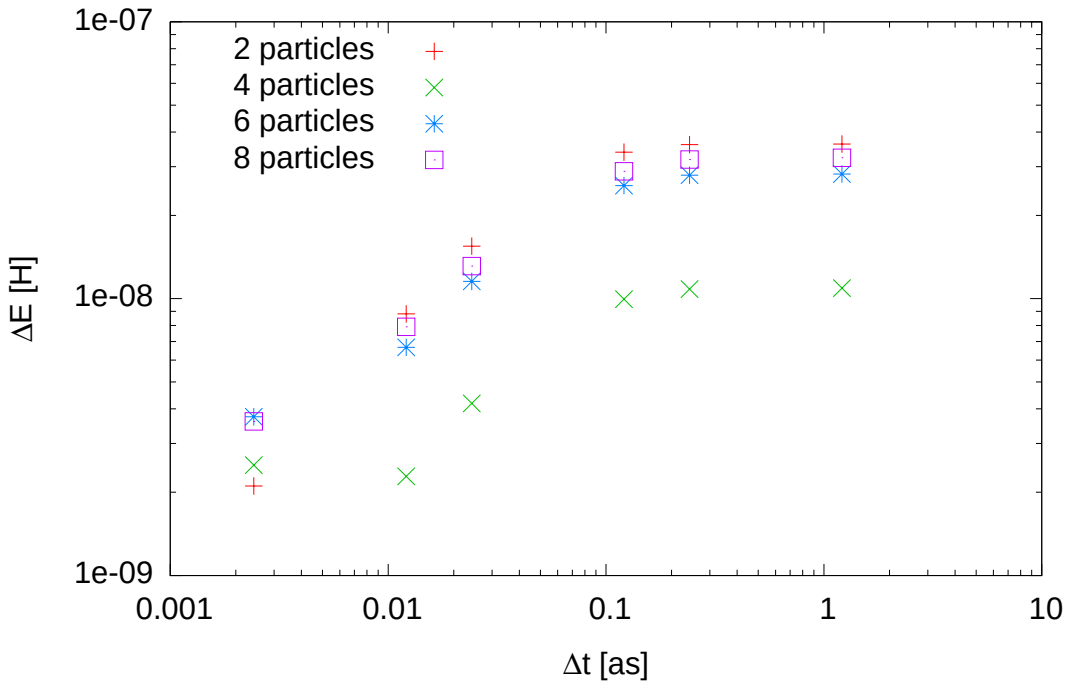

Figure 3.14: The energy drift after about 12 fs as function of the step size for a different number of particles

For the second-order differencing scheme there is a clear dependency of the energy drift on the system size (see figure 3.9). This cannot be observed in here. The smallest system (red) has for all, but the shortest, step sizes the largest energy drift. Furthermore the four particle system (green) has for most of the time steps a notably lower energy drift than the rest of the systems. The reason for these effects are unknown.

However, in all cases the energy drift is less then 10^{-7} fs for the reasonable step size of $\Delta t = 0.24$ as. Thus the time evolution is considered suitable for the quantum harmonic oscillator. Therefore, it will be used to study the response of the quantum harmonic oscillator upon ionization (see 4.1).

3.6.2 Alkanes

The time evolution operator scheme conserves the norm within the numerical precision for the harmonic oscillator. Also the energy drift is small. Therefore the time evolution operator scheme is systematically tested with three-dimensional systems. The first five Alkanes (methane, ethane, propane, n-butane and n-pentane (see 3.3)) are used as a test set of molecules together with the basis sets STO-3G, 6-31G and cc-pVDZ. The step size $\Delta t = 0.24\,\text{as}$ is used.

Figure 3.15 shows the difference ΔE of the energy and the initial energy as a

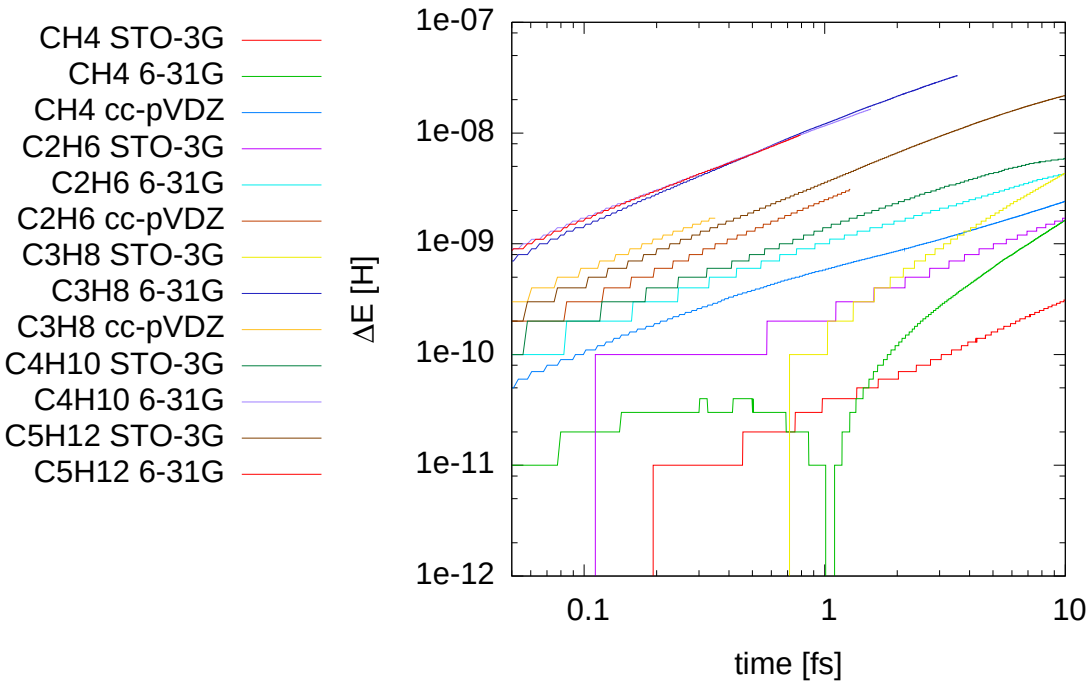

Figure 3.15: Energy drift for the test set of Alkanes with a step size of $\Delta t = 0.24\,\text{as}$ as a function of time

function of time. Some of the trajectories are stopped before 10 fs due to run time limitations. The stair like structure of some of the curves is caused by aliasing effects due to rounding errors.

The larger systems, both with respect to the number of basis functions and the

number of electrons, have a larger energy drift. To see this, consider the ethane molecule. The basis sets consists of 16 (STO-3G, purple), 30 (6-31G, cyan) and 58 (cc-pVDZ, brown). The energy drift is the largest for the cc-pVDZ and the smallest for the STO-3G basis set.

The number of electrons in the molecule also increases the energy drift. Consider the n-butane with the STO-3G basis set (30 basis functions, dark green), the methane with the 6-31G basis set (30 basis functions, cyan) and the methane with the cc-pVDZ basis set (34 basis functions, blue). The n-butane molecule has the largest energy drift and the methane the smallest.

For all cases the energy drift after 10 fs is less then 10^{-7} H. Thus the time evolution operator scheme is considered suitable for three-dimensional systems and will be used to study the response of carbon (see 4.2) and carbon monoxide (see 4.4) to ionization.

3.7 Performance analysis

The code is implemented in ANSI-C. It is worthwhile to test the performance of the code. The program was run on a single core of an Intel Xeon E5430 processor. It was compiled using the Intel `icc` C compiler version 10.1 and linked to the `MKL` version 11.0.

Figure 3.16 compares the performance of the second order differencing and the time evolution operator scheme. The average time needed per integration steps is shown. The error bars indicate the standard deviation of the mean value. The time was averaged over 50 repetitions of 100 integration step.

The time evolution operator scheme needs more matrix multiplications ($O(K^3)$) and the matrix diagonalization ($O(K^3)$) per integration step. Thus it is slower for medium sized basis sets. For large basis sets the difference vanishes because the assembly of the Fock matrix ($O(K^4)$) becomes the dominating step. It has to be assembled in every step in both schemes.

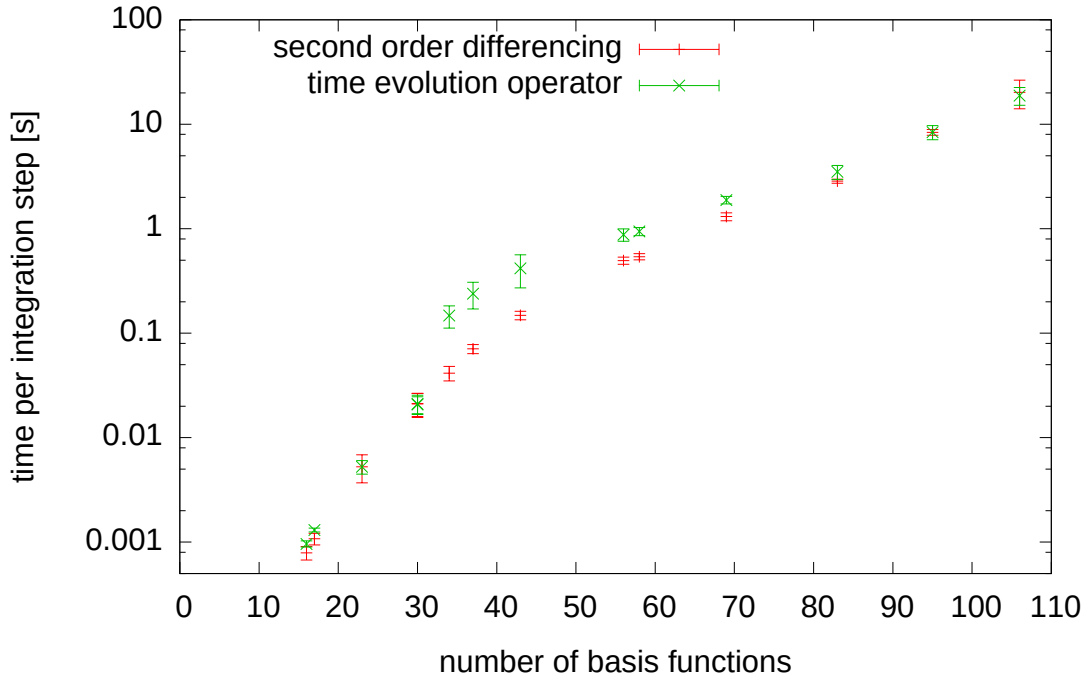

Figure 3.16: Performance of the second order differencing and the time evolution operator scheme. Shown is the time per integration step for varying number of basis functions

There is no obvious explanation for the jump in the time consumption of the time evolution operator scheme between 30 and 34 basis functions. Since we are interested in large systems, this is not further investigated.
Since a larger time step can be used with the time evolution operator scheme, the walltime needed per simulation time is smaller than for the second-order differencing. Thus the time evolution operator scheme is favorable.

3.8 Summary

We have presented three different integration schemes to numerically integrate the time-dependent Hartree-Fock equations within a finite basis set. For all three cases the implementation was briefly described. The integrators were tested for a

one-dimensional test system and atoms and alkane molecules. For all three cases, the time evolution operator scheme was found to be stable. Furthermore, it allows for using a larger integration time step than the second-order differencing scheme and, therefore, provides a better performance.

4

Results

The main process during the interaction of X-ray radiation with biomolecules is photoionization (see chapter 1), which is, therefore, studied in this chapter. Since the photoionization is very fast, it is assumed to be well described by the sudden removal of an electron. In the context of Hartree-Fock theory the removal of the electron is described by removing the corresponding orbital from the Slater determinant (2.3) that describes the ground state of the system. The orbitals are not relaxed to the new situation, but instead the wave function is used as the initial condition for the subsequent time propagation. Because the photoionization mainly removes electrons from the K shell, only removal of the lowest orbitals are studied here. Since after removal the orbitals are no longer eigenfunctions of the Fock operator, we expect a non-trivial time evolution of the wave function, eventually describing the re-filling of the inner shell hole.

In chapter 3 the time evolution operator scheme was found to be stable for both the quantum harmonic oscillator and small molecules. It is therefore used here. The harmonic oscillator is studied first to test the applicability of both the time-dependent Hartree-Fock theory and the integration schemes to describe electron dynamics upon sudden ionization. Then the carbon and the carbon monoxide molecule are taken into account to get insight into more realistic systems.

4.1 Quantum harmonic oscillator

For the propagation of the orbitals, a time step of $\Delta t \approx 0.024\,\text{as}$ is used. Four different cases were studied, with a four, six, eight and ten particle ground state. Of these only the four and the eight particle cases are discussed here in detail; the other two cases show similar results.

Only ionizations from the lowest spin α orbital χ_0^α are considered. The χ_0^α orbital is called the hole orbital in the subsequent sections. Subsequently, the ionization is assumed to occur at $t = 0\,\text{fs}$.

4.1.1 Four particle system

In the Mulliken population analysis the diagonal elements of the density matrix are interpreted as occupation of the corresponding basis functions, see equation (2.28). Figure 4.1 shows the Mulliken populations of the first four basis functions.

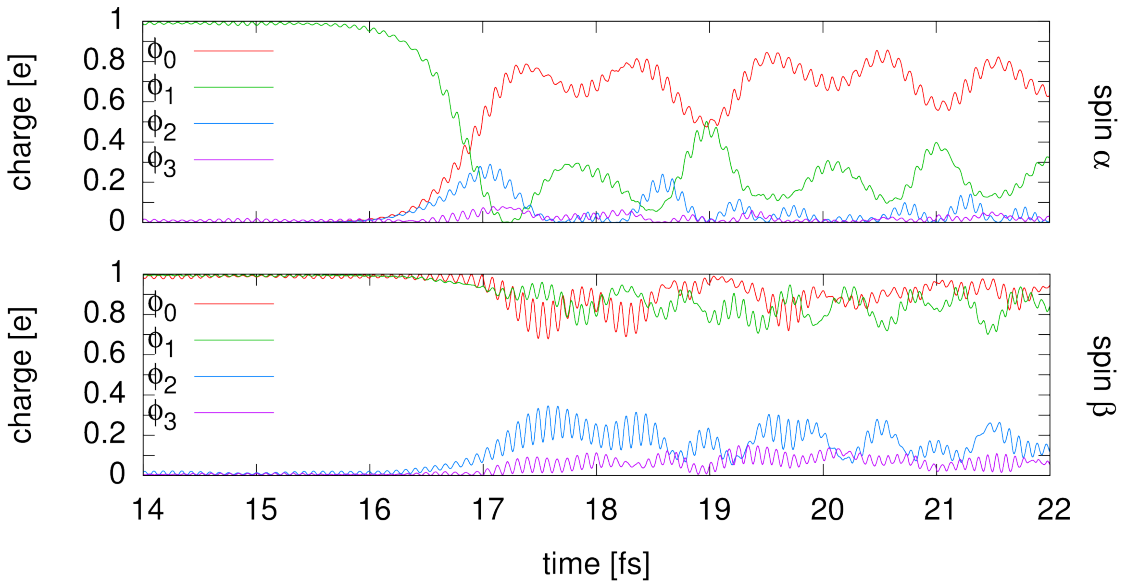

Figure 4.1: Mulliken populations for the spin α (top) and spin β (bottom): at $t = 16\,\text{fs}$ the previously empty basis function ϕ_0 is filled up by the charge from the higher basis function ϕ_1

The higher basis functions are not shown because they remain unoccupied. The first 14 fs are not shown since there is no marked reaction of the system except small oscillations of the occupation of the basis functions. Similar oscillations of the occupations are seen between 14 and 16 fs. At about 16 fs a transition occurs. During the transition, the basis function ϕ_0, which became unoccupied upon the ionization, is re-occupied. The charge is transferred from the higher energy basis function ϕ_1 to the lower ϕ_0. Additionally a smaller fraction of the charge is transferred into the basis functions ϕ_2 and ϕ_3. The spin β orbitals are not affected by the ionization (see figure 4.1), i.e., the two lowest basis functions ϕ_0 and ϕ_1 remain almost completely occupied. The transition at 19 fs also affects the spin β charge. A fraction of the charge is redistributed into the higher basis functions ϕ_2 and ϕ_3. During the process the total energy of the system is conserved. All changes in the occupation of the basis functions are caused by the time evolution of the orbitals.

To follow the time evolution of the time-dependent orbitals $\chi_j(t)$, they are

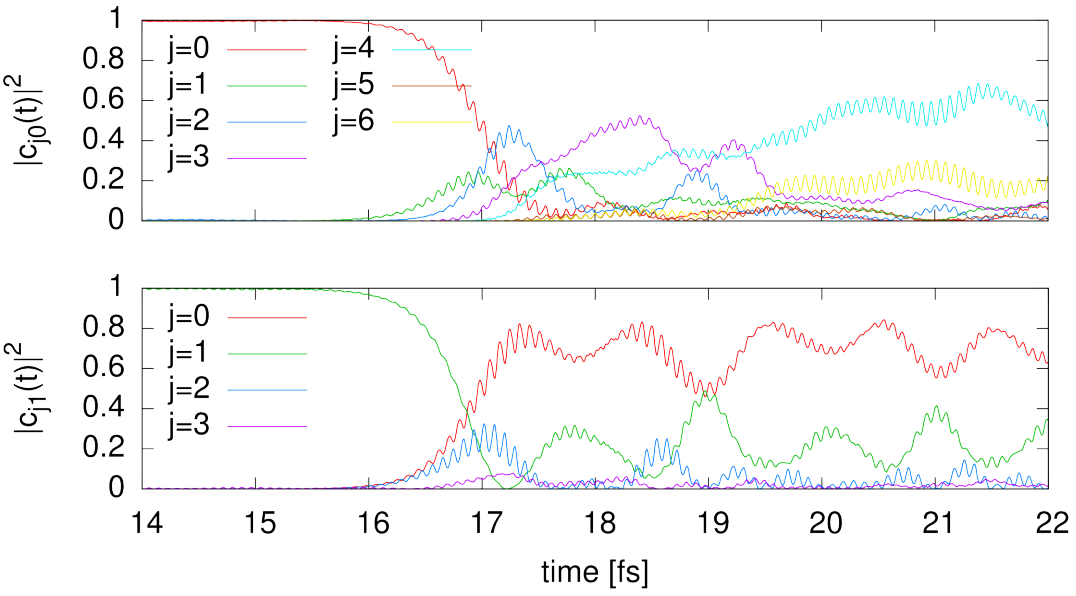

Figure 4.2: Projection of the hole orbital $\chi_0^\alpha(t)$ (top) and the occupied α orbital $\chi_1^\alpha(t)$ (bottom) on the initial orbitals

projected on the initial orbitals $\chi_j(0)$. The projection function is given by

$$\begin{aligned} c_{jk}(t) &= \langle \chi_j(0) | \chi_k(t) \rangle = \\ &= \int \mathrm{d}\mathbf{r} \sum_m^K C^*_{mj}(0) \phi^*_m(\mathbf{r}) \sum_n^K C_{nk}(t) \phi_n(\mathbf{r}) = \\ &= \sum_{mn} C^*_{mj}(0) C_{nk}(t) S_{mn}. \end{aligned} \tag{4.1}$$

Figure 4.2 shows the projection of the hole orbital $\chi_0^\alpha(t)$ and the occupied α orbital $\chi_1^\alpha(t)$ on the initial orbitals. Until the transition at 16 fs the projection functions $c_{00}(t)$ and $c_{11}(t)$ stay almost unity because the orbitals to not change, except for an oscillating phase factor.

During the transition the hole orbital $\chi_0^\alpha(t)$ completely changes its character. At about 18 fs it has become a mixture of the virtual orbitals $\chi_3^\alpha(0)$ and $\chi_4^\alpha(0)$. Afterwards is resembles the virtual orbital $\chi_4^\alpha(0)$, i.e. is has changed its shape completely. The occupied $\chi_1^\alpha(t)$ orbital, in turn, resembles the hole orbital $\chi_0^\alpha(0)$. The particle occupying the orbital $\chi_1^\alpha(t)$ thus fills the hole created by the ionization. After the refilling of the hole, the orbital $\chi_1^\alpha(t)$ oscillates between its original composition $\chi_1^\alpha(0)$ and the composition of the hole orbital $\chi_0^\alpha(0)$. These changes account for the redistribution of the charge that can be seen in the Mulliken population analysis.

Figure 4.3 shows the projection of the occupied orbitals $\chi_0^\beta(t)$ and $\chi_1^\beta(t)$. Compared to the spin α orbitals, the transition occurs about 0.5 fs later at about 17 fs. The orbitals then quickly exchange their composition. Additionally, the orbital $\chi_0^\beta(t)$ acquires a small contribution of the orbitals $\chi_2^\beta(0)$ and $\chi_3\beta(0)$. This causes the occupation of the higher energy basis functions ϕ_2 and ϕ_3 seen in the Mulliken population analysis. The initial transition is not reversed, but the composition of the orbitals $\chi_0^\beta(t)$ and $\chi_1^\beta(t)$ oscillate.

The transition seen after about 17 fs describes the Auger effect. The hole created by the ionization is filled by a particle occupying the highest orbital of the same spin. Energy is not conserved in the transition. The same system was also studied

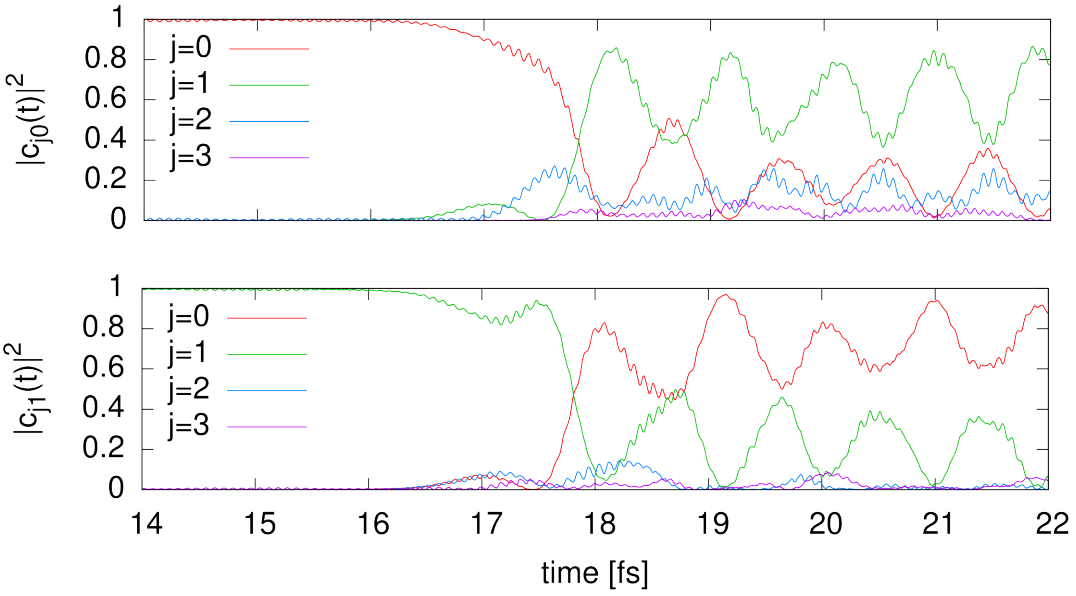

Figure 4.3: Projection of the occupied β orbitals $\chi_0^\beta(t)$ (top) and $\chi_1^\beta(t)$ (bottom) on the initial orbitals

using the second-order difference scheme with a time step of $\Delta t \approx 0.024\,\text{as}$. Similar processes, including the Auger-like transitions, are observed. In contrast to the time evolution operator scheme, the second-order difference scheme conserves energy. The energy fluctuates about within a range of $\Delta E/E(0) \approx 10^{-4}$. This indicates that the Auger-like transition is not an artifact caused by inaccuracies of the time evolution operator scheme. Possible reasons for the violation of the energy conservation are discussed in 4.5.

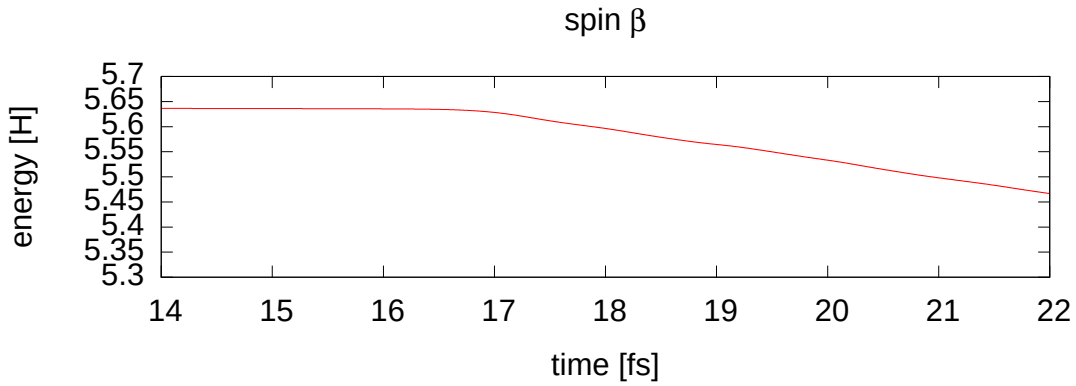

Figure 4.4: Energy as a function of time: at $t = 17\,\mathrm{fs}$, i.e. in the transition, the energy drifts

4.1.2 Eight particle system

Figure 4.5 shows the Mulliken populations for the lowest six basis functions and spin α. Like in the four particle case, there is a delay before the system show a notable response to the ionization, except small oscillations. The same oscillation can be seen in the figure 4.5 between 8 and about 10 fs. Thus the first 8 fs are not shown. At about $t = 10$ fs a transition occurs. Similar to the four particle case

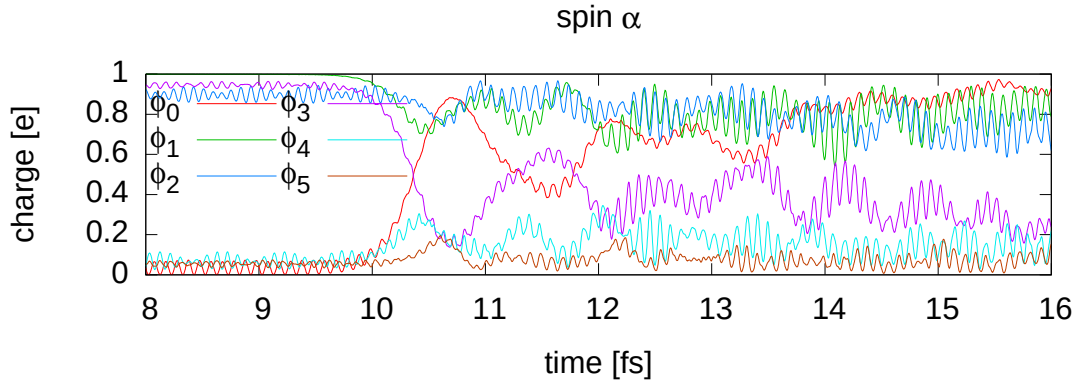

Figure 4.5: Mulliken populations for the spin α: the previously empty basis function ϕ_0 gets occupied by charge coming from the basis function ϕ_3

the basis function ϕ_0 is filled up within 1 fs. The charge is transferred mainly from the ϕ_3 to the ϕ_0 basis function. Simultaneously the occupation of the basis functions ϕ_1 and ϕ_2 decreases by about 20%. While, the basis functions ϕ_4 and ϕ_5 become partially occupied. After the first fast transition the occupations of the basis functions strongly oscillate. At about $t = 14$ fs the occupation of ϕ_0 has increased to about 0.9 e and does not oscillate anymore. However, the occupation of the other basis functions still shows fast oscillations with a period of about 100 as.

The charge transfer is driven by the orbital dynamics. During the transition the hole orbital $\chi_0^\alpha(t)$ (figure 4.6) and the occupied orbital $\chi_3^\alpha(t)$ (figure 4.9) exchange their composition. Also the following oscillations of the charge seen in the

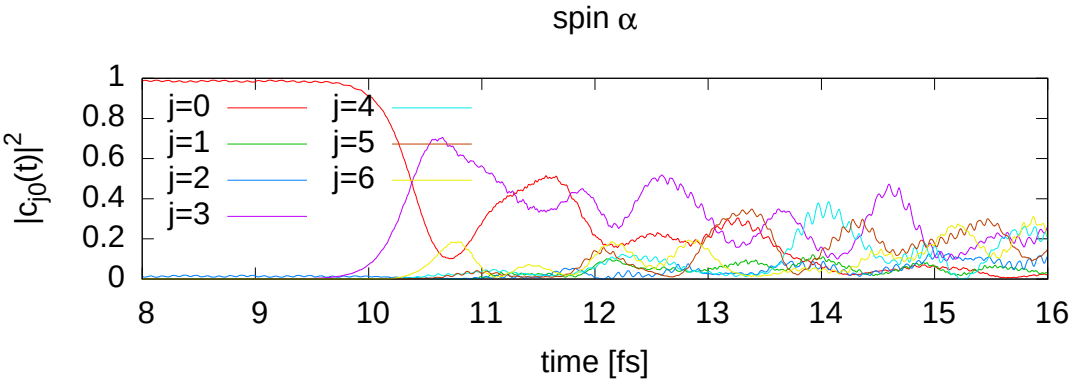

Figure 4.6: Projection of the hole orbital $\chi_0^\alpha(t)$ on the initial orbitals

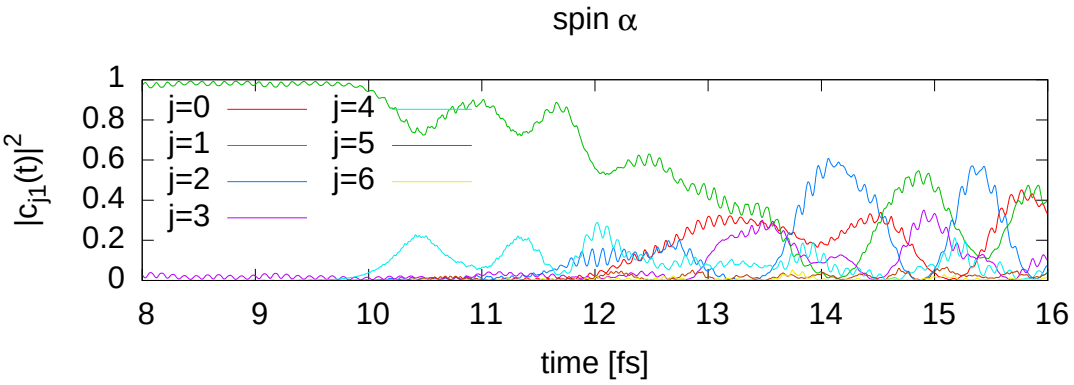

Figure 4.7: Projection of the orbital $\chi_1^\alpha(t)$ on the initial orbitals

Mulliken population analysis are visible in the projection of the orbital $\chi_0^\alpha(t)$ and $\chi_3^\alpha(t)$ at about 11.5 fs. After 14 fs the hole orbital has completely lost its original composition. The virtual orbitals $\chi_4^\alpha(0)$, $\chi_5^\alpha(0)$ and $\chi_6^\alpha(0)$ contribute most to the projection of $\chi_0^\alpha(t)$. This means, that the hole orbital it then mostly composed of the higher energy basis functions.

After about 12 fs the initial state in which each orbital is mostly composed by the corresponding basis function has completely decayed. The three occupied orbitals are composed from the three lowest orbitals. However, the exact contributions of the basis functions to the orbitals are oscillating.

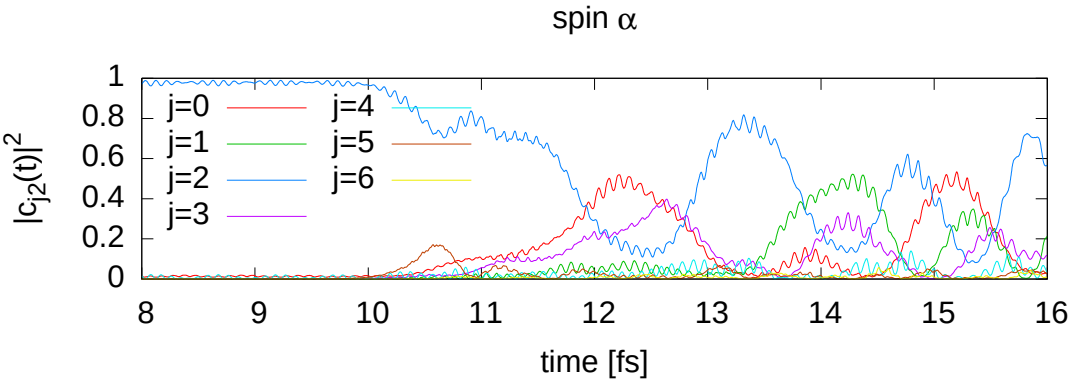

Figure 4.8: Projection of the orbital $\chi_2^\alpha(t)$ on the initial orbitals

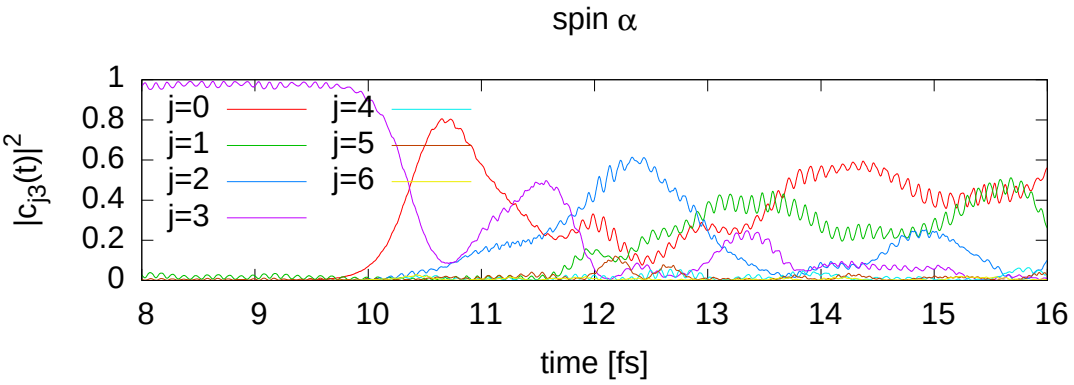

Figure 4.9: Projection of the orbital $\chi_3^\alpha(t)$ on the initial orbitals

Figure 4.10 shows the Mulliken populations for spin β. The transition is delayed by about 0.5 fs compared to the spin α case. During the transition charge is transferred form the occupied basis functions ϕ_1, ϕ_2 and ϕ_3 into the higher basis functions ϕ_4 and ϕ_5. After this initial transition the occupation of the basis functions shows fast oscillations with a period of about 100 as like in the spin α case. After about 15 fs a fraction of the charge from the basis functions ϕ_2 and ϕ_3 is transfered to the basis function ϕ_4.

At about $t = 11$ fs the orbitals $\chi_0^\beta(t)$ (figure 4.11) and $\chi_3^\beta(t)$ (figure 4.14) have partially exchanged their shape. This is similar to the situation in the four

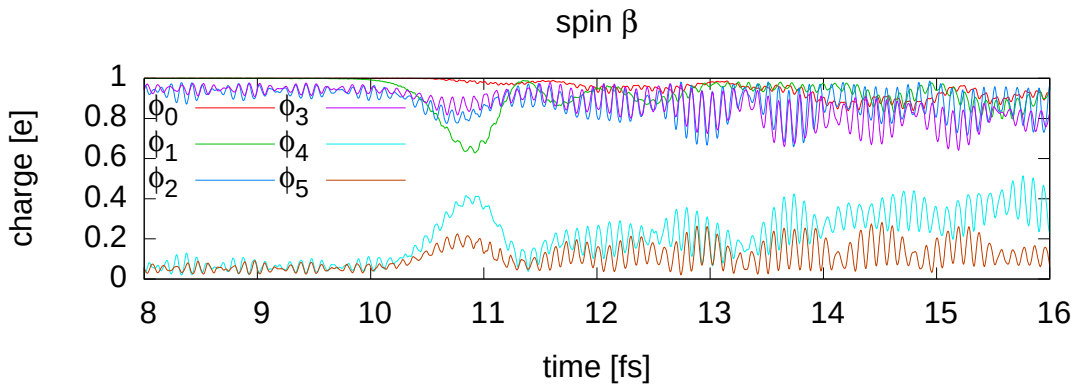

Figure 4.10: Mulliken populations for the spin β: The charge from the occupied basis function gets redistributed into higher basis functions

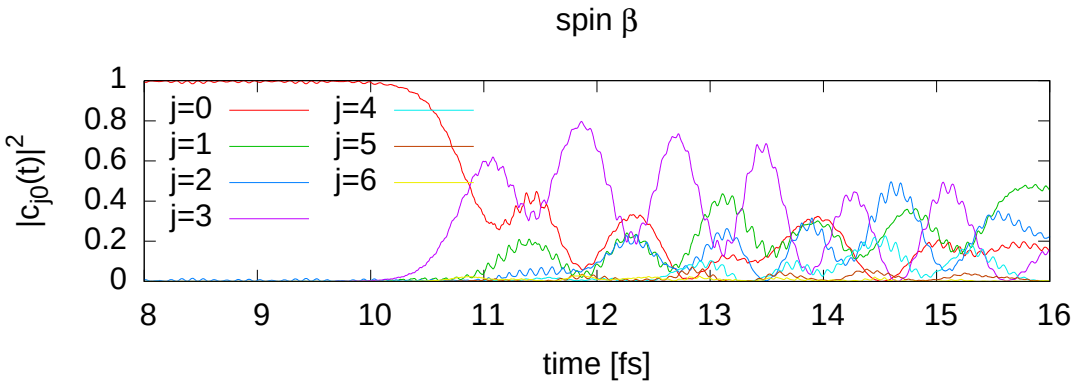

Figure 4.11: Projection of the orbital $\chi_0^\beta(t)$ on the initial orbitals

particle case where the occupied β orbitals almost completely exchange.

After 13 fs the orbital $\chi_1^\beta(t)$ (figure 4.12) has almost become identical to the initial orbital $\chi_0^\beta(0)$. Thus, it is mostly composed from the ϕ_0 basis function.

After about 14 fs the basis function ϕ_4 contributes to the orbitals $\chi_0^\beta(t)$ and $\chi_3^\beta(t)$. This causes the charge transfer into the basis function ϕ_4 that is visible in the Mulliken population analysis.

Like in the four particle case a refilling of the initially created hole is observed by a particle occupying the highest spin α orbital. The redistribution of charge to

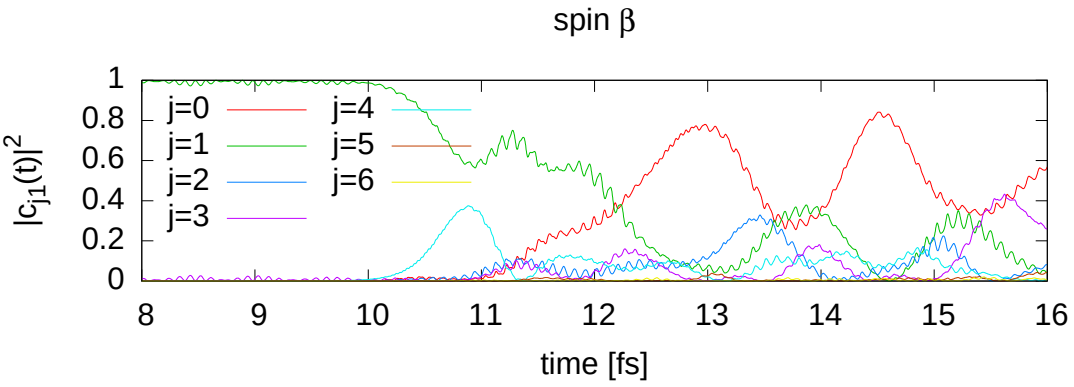

Figure 4.12: Projection of the orbital $\chi_1^\beta(t)$ on the initial orbitals

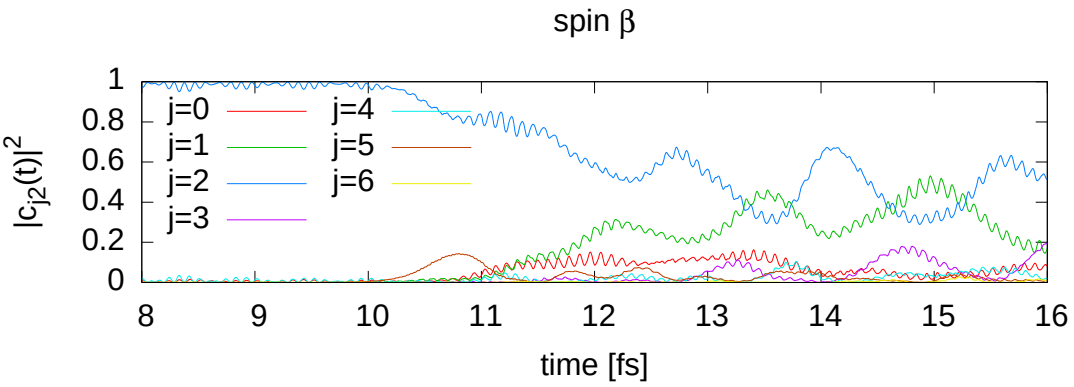

Figure 4.13: Projection of the orbital $\chi_2^\beta(t)$ on the initial orbitals

higher basis functions is more pronounced in this case. Thus again an Auger-like effect is observed.

In more realistic potentials the escaping electron would have to enter the continuum. The harmonic potential does not allow for complete ionization because there are no unbound states. There are no unbound states since the harmonic potential is not bounded.

The Auger-like process was not only observed for the two cases shown here, but also for ionizations of six and ten particle ground states. The delay before the Auger-like process is different for all four cases. However, the delay time seems

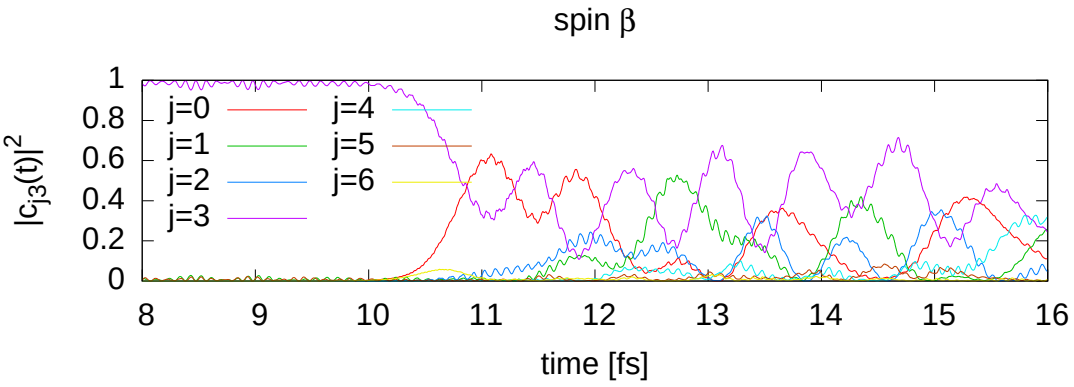

Figure 4.14: Projection of the orbital $\chi_3^\beta(t)$ on the initial orbitals

to be related to the number of particles. In the six particle cases the delay is the shortest with about 1 fs. In the four particle case it is the longest with about 19 fs. In the ten particle case the delay is almost as short as in the six particle case and the eight particle case is in between. In all cases the hole is filled by the highest orbital of the same spin.

4.2 Carbon

To study how full ionization is described in a more realistic, three-dimensional, system, we no consider the carbon atom (see chapter 3.2). The 6-31G basis set is used with a time step of $\Delta t = 0.24\,\text{as}$. The atom $1\sigma^{\alpha}$ orbital is ionized. Although stable in the test with the closed shell systems (see chapter 3.6.2), the time evolution operator scheme turns out to be unstable in this open shell system. This effect is discussed in section 4.3. Thus, we restrict our analysis to the first fs of the time evolution.

Figures 4.15 and 4.16 show the Mulliken population for both spin α and β of

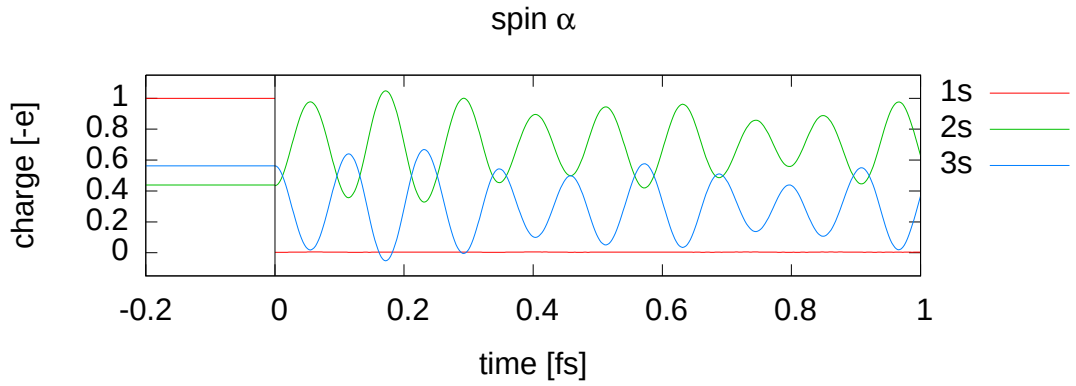

Figure 4.15: Mulliken population analysis of the three s-type basis functions shown for spin α

selected orbitals. Since the changes in spin α and spin β are the same, not all basis functions are shown in each plot.

The ionization takes place at $t = 0\,\text{fs}$, as indicated by the vertical line. Before the ionization, the occupation of the basis functions does not change. That means the orbitals do not change except for an oscillating phase factor.

In contrast to the delay observed for the harmonic oscillator (see chapter 4.1), the system immediately reacts to the ionization. For both spins the charge oscillates between basis functions of the same angular momentum, i.e. between $2s$ and $3s$,

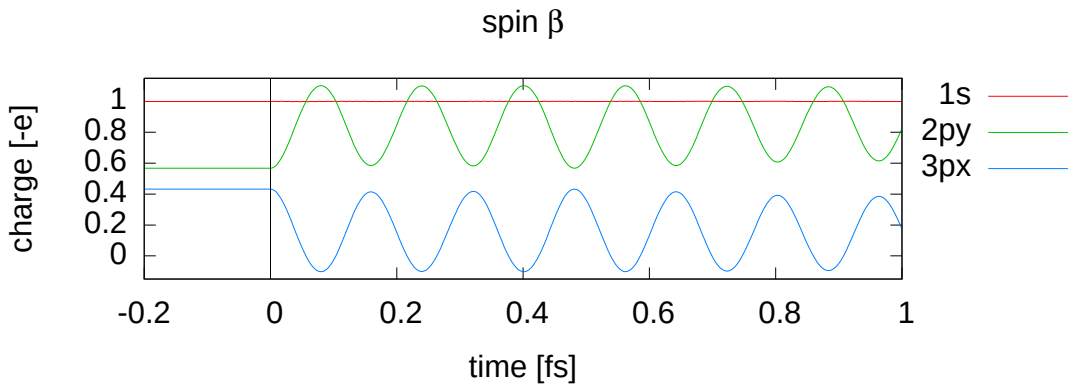

Figure 4.16: Mulliken population analysis of the lowest s-type and two p-type basis functions shown for spin β

and $2py$ and $3px$. The occupation of the $1s$ basis function is not affected. In the spin α case the spin α basis function remains empty and in the spin β case filled. Figure 4.17 shows the time evolution of the charge density of two orbitals. The orbitals are interpreted as single particle wave functions. The charge density

$$\begin{aligned}\rho_j(t_0,\mathbf{r}) &= \int \mathrm{d}\mathbf{r}|\psi_j(t_0,\mathbf{r})|^2 = \psi_j(t_0,\mathbf{r})^*\psi_j(t_0,\mathbf{r}) \\ &= \sum_{mn} C^*_{mj}(t_0)C_{nj}(t_0)\int \mathrm{d}\mathbf{r}\phi^*_m(\mathbf{r})\phi_n(\mathbf{r}) \\ &= \sum_{mn} C^*_{mj}(t_0)C_{nj}(t_0)S_{mn}(\mathbf{r}). \end{aligned} \tag{4.2}$$

created by an electron occupying the orbital is evaluated. The plots were created with the `VMD` program [15].

As can be seen, both orbitals contract and expand periodically reflecting the charge oscillation. However, within this short time frame of 1 fs, the $1\sigma^\alpha$ orbital does not change. The $1s$ basis function is not reoccupied either.

The 1σ orbital is spherical and dense compared to the higher energy orbitals. Thus, the electrons occupying the 1σ orbital screen the charge of the nucleus. The ionization removes one of the 1σ electrons. Thus the effective charge seen by the other electrons increases. Directly after the ionization the charge is trans-

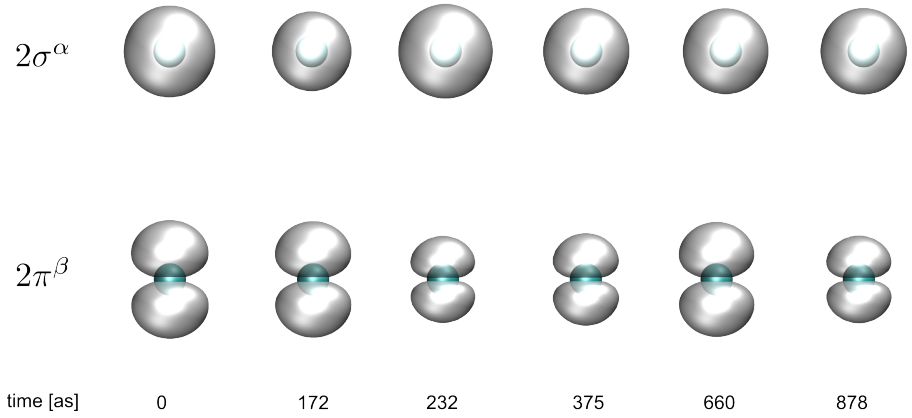

Figure 4.17: Time evolution of the $2\sigma^{\alpha}$ and $2\pi^{\beta}$ orbital as isosurface

ferred to lower energy basis functions, which are dense near to the nucleus. As a consequence, the potential energy of the system is reduced. At the same time the occupied orbitals are contracted. Thus, the kinetic energy, which is proportional to the curvature of the orbitals, increases. The total energy is conserved in this process during the first 1 fs. The carbon atom has a core hole life time of about 11.1 fs [16] in the Auger effect. Thus an Auger-like transition is not expected within the first femtosecond. A longer time scale than 1 fs is studied in the subsequent section.

4.3 Beyond 1 fs: Numerical instabilities

Since the Auger effect has a longer life time than 1 fs a longer time scale has to be reached. Figure 4.18 shows the Mulliken populations for spin α and spin β.

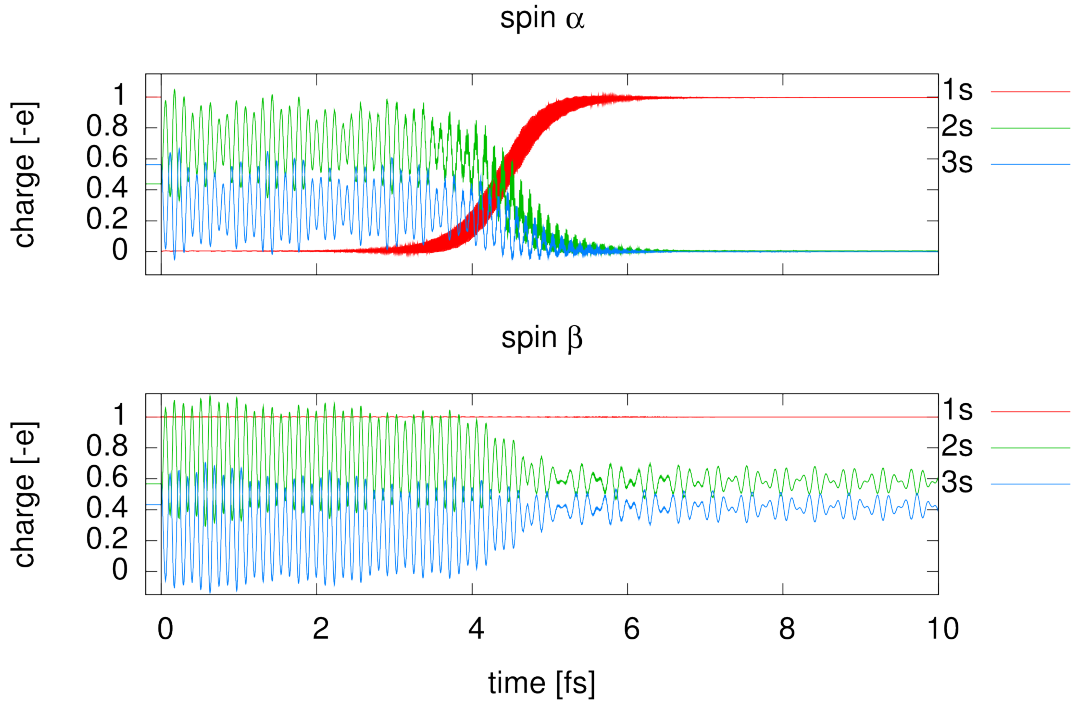

Figure 4.18: Mulliken populations for carbon and spin α (top) and spin β (bottom) as a function of time

For convenience, only the basis functions with the most pronounced change in occupation are shown. At about 4 fs a transition is seen. For spin α (figure 4.18), charge is transfered from the basis functions $2s$ and $3s$ to the previously empty basis function $1s$. Simultaneously the charge is transfered from the $2s$ to the $3s$ basis function in spin β. This resembles the Auger-like effect that is observed for the harmonic oscillator (see chapters 4.1.1 and 4.1.2).
However, the energy conservation is violated during the transition. This can be seen from figure 4.19 where the total energy is shown as a function of time for three different time steps. For step size $\Delta t \approx 0.24$ as, energy conservation is

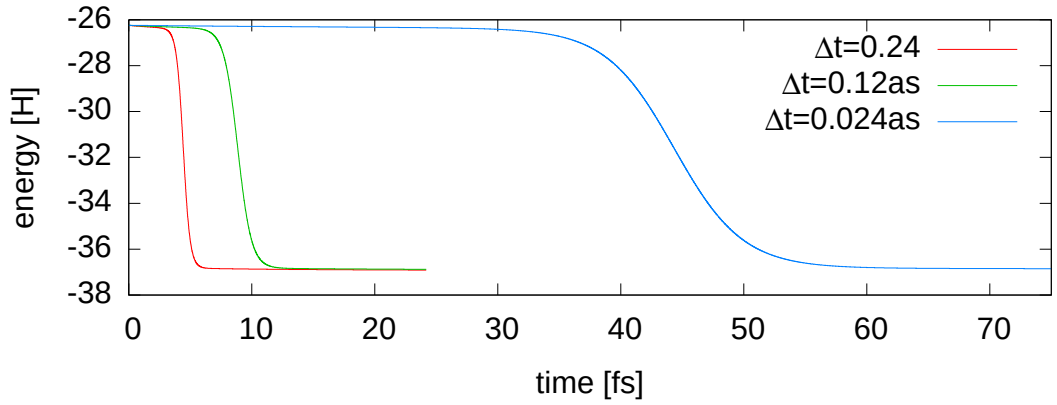

Figure 4.19: The total energy as a function of for three different step size

violated during the transition described above occurs. For the other two step sizes similar transitions are observed at the time when the energy conservation is violated. The life time depends on the integration step used. The increase in life time for the smaller time step is proportional to the decrease in the step size. This indicates that the transition is caused by an instability of the integration scheme and is thus an artifact (see chapter 4.5).

The norm conservation is not affected by the transition. Before the transition, also the energy is conserved. Thus the time evolution operator scheme is considered stable before the transition. Accordingly, the results obtained in 4.2 are not affected by the instability.

4.4 Carbon monoxide

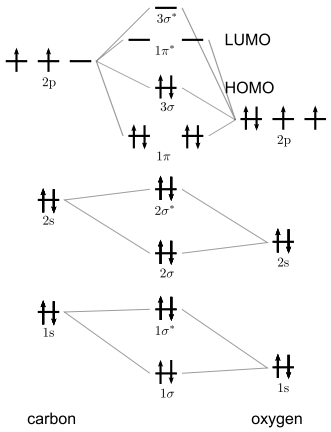

Figure 4.20: Molecular orbital diagram of carbon monoxide

Due to the instabilities observed in the previous section, the analysis of the time evolution is limited to the first 1 fs. During the first femtosecond no transition is observed and the energy is conserved within $\Delta E/E(0) = 0.002$. The molecular orbital diagram of carbon monoxide is shown in figure 4.20. Two cases are considered here, the ionization from the 1σ orbital which mostly resides at the oxygen atom, and the ionization from the $1\sigma^*$ orbital which mostly resides at the carbon atom.

Again the 6-31G basis set is used. The Mulliken charge analysis is shown instead of the population analysis, because the 6-31G basis set for carbon monoxide consists of 18 basis function and a Mulliken population analysis is, therefore, inconvenient.

The Mulliken charge analysis is obtained by summing up the charge of all basis functions centered at the same nucleus. From the charge analysis before the ionization the initial dipole moment of carbon monoxide can be seen (figure 4.21). However, it has the wrong orientation. This is one of the well known deficiencies of the Hartree-Fock theory [5].

Also here the time evolution operator scheme suffers from instabilities. Thus, only the first femtosecond of time evolution is shown.

4.4.1 Ionization of 1σ orbital

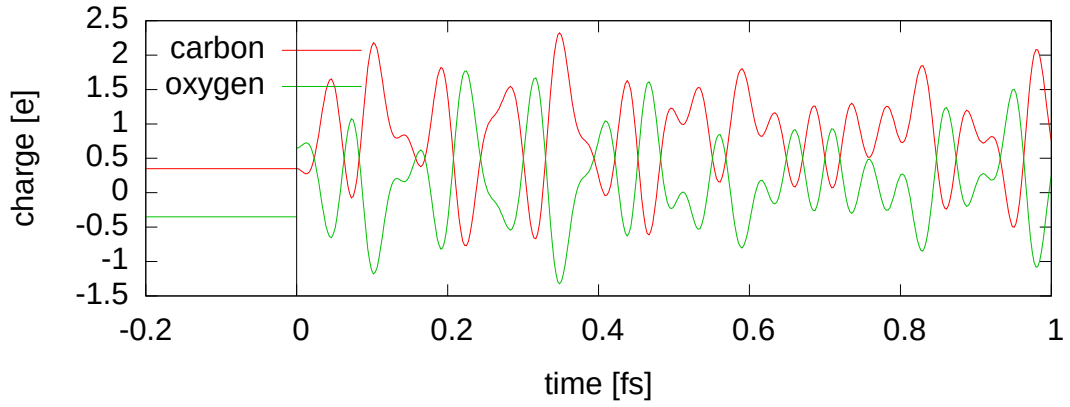

Figure 4.21: Mulliken charges during the first 1 fs

Figure 4.21 shows the Mulliken charge analysis. The charge of the oxygen atom raises by one upon ionization because the 1σ orbital is mostly composed from the $1s$ basis function centered at the oxygen. Thus it more strongly attracts the remaining electrons. This causes the charge to oscillate between the nuclei. The oscillation has a period of about 40 as. This corresponds to radiation with a wave length of $\lambda \approx 12\,\text{nm}$.

No refilling of the empty oxygen $1s$ basis function can be observed. Figure 4.22

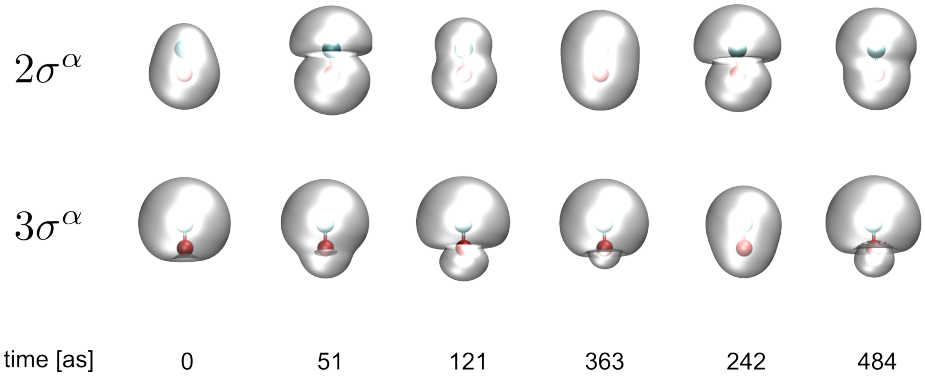

Figure 4.22: Isosurfaces of the orbitals $2\sigma^\alpha$ and $3\sigma^\alpha$ at different times

shows isosurface plots of the orbitals $2\sigma^{\alpha}$ and $3\sigma^{\alpha}$. As can be seen, the electron density oscillates between the nuclei.

4.4.2 Ionization of $1\sigma^{*}$ orbital

The $1\sigma^{*}$ orbital is mainly composed from the $1s$ basis function centered at the carbon atom. Thus the charge of the carbon raises by one upon ionization. Like

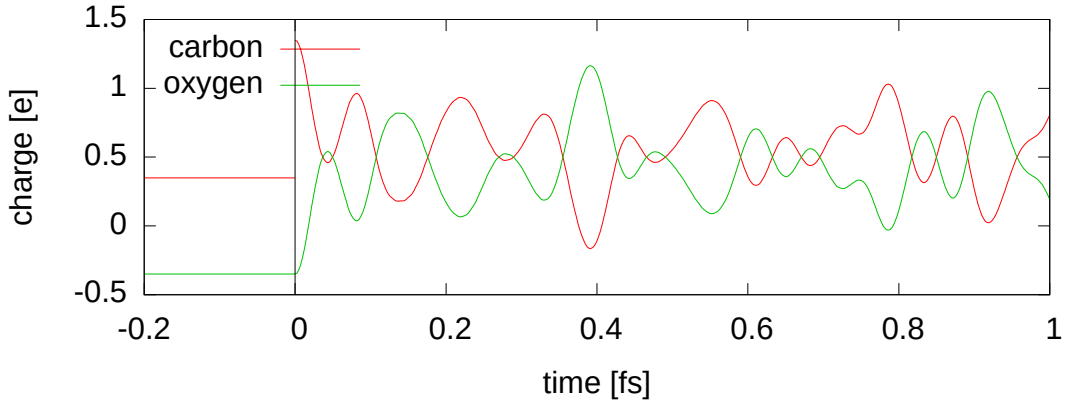

Figure 4.23: Mulliken charge analysis throughout 1 fs

for the ionization from the 1σ orbital, the charge immediately starts oscillating between the nuclei. The oscillation is weaker because the 1σ orbital does not change significantly. Because the electrons occupying the 1σ orbital are tightly bound to the oxygen atom. Also in this case no change of the hole orbital or refilling of the carbon $1s$ basis function can be observed within 1 fs.
In both cases the charge first oscillates towards the ionized atom. Thus the time-dependent Hartree-Fock theory gives a reasonable response of the system to the ionization also for this more complex system. The core hole life time of oxygen in the Auger transition is about 6.6 fs [16]. Accordingly, to transition is expected in the first femtosecond.

4.5 Discussion

In the harmonic potential a spontaneous refilling of the core hole is observed. Simultaneously charge is redistributed into higher orbitals. This process resembles what is expected during an Auger process. The carbon atom and the carbon monoxide molecule immediately respond to the ionization. The charge oscillates between different orbitals. In the carbon monoxide molecule this results in an oscillating dipole moment.

For the carbon atom a transition is observed. During this transition the hole is filled. While electrons of the opposite spin occupy higher energy basis functions. However, the energy is not conserved as it should.

We can see three possible reasons for the violation of the energy conservation. The time evolution operator (see equation (2.41)) is unitary. This ensures norm conservation during the time propagation. Since the Fock operator is time-dependent, the norm conservation does not imply the conservation of the expectation value of the Fock operator. The expectation value is only conserved, if the Fock operators at different times commute. Similarly the energy, which is not the energy of the Fock operator, is only conserved if the Hamiltonian commutes with the Fock operator.

A numerical solution of the time-dependent Hartree-Fock equations will only yield norm and energy conservation with a finite accuracy imposed by the integrator deployed. Thus a suitable integrator has to be used, to keep the errors caused by the approximations within a reasonable range. Both the second-order differencing and the time evolution operator scheme exhibit deficiencies, so further researcj in this direction is clearly required.

The second-order differencing scheme clearly fails in the application to the carbon atom. It is not strictly unitary, which causes the norm to grow rapidly, as can be seen from figures 3.10 and 3.11. In the case of the harmonic oscillator the

norm and energy drifts are within an acceptable range. This is due to the weaker interaction between the particles. The Coulomb repulsion between electrons is not bounded, whereas the model potential (see equation (3.2)) stays finite for all particle-particle distances.

The time evolution operator scheme is unitary. Accordingly, in all cases seen so far the norm is conserved. However, it violates the energy conservation in the transition observed for both the harmonic oscillator and the carbon atom. The effect is more pronounced for the carbon. This effect may be due to the stronger Coulomb interaction.

Unfortunately we observed that the life time of the decay is proportional to the step size used for the integration and therefore is likely caused by the first order approximation of the integral in the time evolution operator (see equation (2.41)) in equation (3.1).

It is of course, finally, possible, that - despite extensive testing - the problems seen for both the second-order differencing and the time evolution operator scheme are caused by programming errors.

5

Conclusion & Outlook

We have shown that time-dependent Hartree-Fock theory is capable of describing the decay of a core ionized state in a harmonic model system. The ionized state was found to decay in an Auger-like process. The application to more realistic systems could not be judged so far because the analysis has to be limited to the first femtosecond after the ionization due to numerical violation of the energy conservation. This violation is most likely caused by still not sufficiently accurate integration schemes or mistakes in the implementation. The response to the ionization of both the carbon atom and the carbon monoxide in the first femtosecond was rationalized.

Instead of directly going from closed shell to directly open inner shell systems, situation should be considered where the initial state is perturbed less. The time evolution of excited states is a starting point for further analysis.

To study larger systems, the performance of the implementation has to be improved considerably. The most time consuming step for larger systems is the formation of the Fock matrix. To increase the performance of the formation of the Fock matrix, the integration schemes will be implemented into a quantum chemistry program. So it is possible to use the optimized routines for this task. Furthermore, it is then possible to use direct SCF schemes. Thus the two electron

integrals do not have to be stored in memory anymore and the system size is not limited by the memory anymore like in the current implementation. This also offers the possibility to use correlated methods, if the time-dependent Hartree-Fock theory turns out to be insufficient for the three-dimensional systems. However, this would again strongly limit the achievable system size.

What is missing in the currently used basis sets, is the description of an unbound electron. When studying the Auger effect, the wave function of the escaping electron needs to be modeled with a finite basis set. But the basis sets used so far are designed to describe only bound states. It is therefore necessary to use additional basis functions. Two different approaches have been used to construct a basis set for an unbound electron. Cederbaum et al. [4] use a grid of gaussian basis functions. The grid was constructed to resemble a large s-type wave function. This approach has the advantage of using a pure gaussian basis. The second possibility are hybrid basis sets in which the unbound electron is described by plane waves. This approach has, for instance, been used to calculate photoelectron spectra [17]. In future work we would like to test which of these two approaches performs better for the systems at hand.

Bibliography

[1] KENDREW, J., BODO, G., DINTZIS, H., PARRISH, R., WYCKOFF, H., and PHILLIPS, D. *NATURE* **181**, 662–666 (1958).

[2] Neutze, R., Wouts, R., van der Spoel, D., Weckert, E., and Hajdu, J. *NATURE* **406**, 752–757 (2000).

[3] Hau-Riege, S., London, R., and Szoke, A. *PHYSICAL REVIEW E* **69** (2004).

[4] Kuleff, A. I. and Cederbaum, L. S. *PHYSICAL REVIEW LETTERS* **98** (2007).

[5] Szabo, A. and Ostlund, N. S. *Modern Quantum Chemistry.* McGraw-Hill, (1989).

[6] Dirac, P. *PROCEEDINGS OF THE CAMBRIDGE PHILOSOPHICAL SOCIETY* **26**, 376–385 (1930).

[7] Raab, A. *CHEMICAL PHYSICS LETTERS* **319**, 674–678 (2000).

[8] MCLACHLAN, A. *MOLECULAR PHYSICS* **8**, 39–& (1964).

[9] NEWTON, M., LATHAN, W., HEHRE, W., and POPLE, J. *JOURNAL OF CHEMICAL PHYSICS* **52**, 4064–& (1970).

[10] DILL, J. and POPLE, J. *JOURNAL OF CHEMICAL PHYSICS* **62**, 2921–2923 (1975).

[11] Frisch, M. J., Trucks, G. W., Schlegel, H. B., andM. A. Robb, G. E. S., Cheeseman, J. R., Montgomery, Jr., J. A., andK. N. Kudin, T. V., Burant, J. C., Millam, J. M., Iyengar, S. S., andV. Barone, J. T., Mennucci, B., Cossi, M., Scalmani, G., andG. A. Petersson, N. R., Nakatsuji, H., Hada,

M., Ehara, M., andR. Fukuda, K. T., Hasegawa, J., Ishida, M., Nakajima, T., Honda, Y., andH. Nakai, O. K., Klene, M., Li, X., Knox, J. E., Hratchian, H. P., andV. Bakken, J. B. C., Adamo, C., Jaramillo, J., Gomperts, R., andO. Yazyev, R. E. S., Austin, A. J., Cammi, R., Pomelli, C., andP. Y. Ayala, J. W. O., Morokuma, K., Voth, G. A., Salvador, P., andV. G. Zakrzewski, J. J. D., Dapprich, S., Daniels, A. D., andO. Farkas, M. C. S., Malick, D. K., Rabuck, A. D., andJ. B. Foresman, K. R., Ortiz, J. V., Cui, Q., Baboul, A. G., andJ. Cioslowski, S. C., Stefanov, B. B., Liu, G., Liashenko, A., andI. Komaromi, P. P., Martin, R. L., Fox, D. J., Keith, T., andC. Y. Peng, M. A. A.-L., Nanayakkara, A., Challacombe, M., andB. Johnson, P. M. W. G., Chen, W., Wong, M. W., Gonzalez, C., and Pople, J. A. Gaussian, Inc., Wallingford, CT, 2004.

[12] Binkley, J. S., Pople, J. A., and Hehre, W. J. *Journal of the American Chemical Society* **102**, 939–947 (1980).

[13] Atkinson, K. E. *An Introduction to Numerical Analyis*. Wiley, (1988).

[14] ASKAR, A. and CAKMAK, A. *JOURNAL OF CHEMICAL PHYSICS* **68**, 2794–2798 (1978).

[15] Humphrey, W., Dalke, A., and Schulten, K. *Journal of Molecular Graphics* **14**, 33–38 (1996).

[16] KRAUSE, M. and OLIVER, J. *JOURNAL OF PHYSICAL AND CHEMICAL REFERENCE DATA* **8**, 329–338 (1979).

[17] Seabra, G., Kaplan, I., Zakraewski, V., and Ortiz, J. *JOURNAL OF CHEMICAL PHYSICS* **121**, 4143–4155 (2004).

A

Appendix

A.1 Calculation

Here the calculations of the relations (2.36), (2.37) and (2.38), which were skipped, in 2.3 are shown.

$$
\begin{aligned}
\langle \delta\Psi | \partial_t | \Psi \rangle = & \int \mathrm{d}\mathbf{x}_1 \cdots \mathrm{d}\mathbf{x}_N \frac{1}{N!} \sum_{\sigma \in S_N} \operatorname{sgn}(\sigma) \sum_j^N \delta\chi^*_{\sigma(j)}(\mathbf{x}_j) \prod_{k \neq j}^N \chi^*_{\sigma(k)}(\mathbf{x}_k) \times \\
& \sum_{\pi \in S_N} \operatorname{sgn}(\pi) \sum_l^N \partial_t \chi_{\pi(l)}(\mathbf{x}_l) \prod_{m \neq l}^N \chi_{\pi(m)}(\mathbf{x}_m) \\
= & \int \mathrm{d}\mathbf{x}_1 \cdots \mathrm{d}\mathbf{x}_N \frac{1}{N!} \sum_{\sigma \in S_N} \operatorname{sgn}(\sigma) \sum_j^N \delta\chi^*_{\pi\circ\sigma(j)}(\mathbf{x}_j) \prod_{k \neq j}^N \chi^*_{\pi\circ\sigma(k)}(\mathbf{x}_k) \times \\
& \sum_{\pi \in S_N} \operatorname{sgn}(\pi) \sum_l^N \partial_t \chi_{\pi(l)}(\mathbf{x}_l) \prod_{m \neq l}^N \chi_{\pi(m)}(\mathbf{x}_m) \\
= & \int \mathrm{d}\mathbf{x}_1 \cdots \mathrm{d}\mathbf{x}_N \sum_{\sigma \in S_N} \sum_k^N \delta\chi^*_{\sigma(j)}(\mathbf{x}_j) \prod_{k \neq j}^N \chi^*_{\sigma(k)}(\mathbf{x}_k) \times \\
& \sum_l^N \partial_t \chi_l(\mathbf{x}_l) \prod_{m \neq l}^N \chi_m(\mathbf{x}_m)
\end{aligned}
$$

Here the group property of S_N has been used to eliminate the first sum over S_N.

$$
\begin{aligned}
&= \int \mathrm{d}\mathbf{x}_1 \cdots \mathrm{d}\mathbf{x}_N \sum_{\sigma\in S_N} \sum_{j,l}^{N} \Bigg\{ \delta_{jl}\delta\chi^*_{\sigma(j)}(\mathbf{x}_j)\partial_t\chi_j(\mathbf{x}_j) \prod_{k\neq j}^{N} \chi^*_{\sigma(k)}(\mathbf{x}_k)\chi_k(\mathbf{x}_k 0) + \\
&\quad (1-\delta_{jl})\delta\chi^*_{\sigma(j)}(\mathbf{x}_j)\chi_j(\mathbf{x}_j)\chi^*_{\sigma(l)}(\mathbf{x}_l)\partial_t\chi_l(\mathbf{x}_l) \prod_{k\neq j,l}^{N} \chi^*_{\sigma(k)}(\mathbf{x}_k)\chi_k(\mathbf{x}_k) \Bigg\} \\
&= \sum_{\sigma\in S_N} \sum_{j}^{N} \prod_{k\neq j}^{N} \delta_{\sigma(k)k} \int \mathrm{d}\mathbf{x}_j \delta\chi^*_{\sigma(j)}(\mathbf{x}_j)\partial_t\chi_j(\mathbf{x}_j) \\
&= \sum_{j}^{N} \int \mathrm{d}\mathbf{x}_j \delta\chi^*_j(\mathbf{x}_j)\partial_t\chi_j(\mathbf{x}_j) \\
&= \sum_{j}^{N} \langle \delta\chi_j | \partial_t | \chi_j \rangle
\end{aligned}
\tag{A.1}
$$

The equation

$$
\langle \delta\Psi | \sum_{j}^{N} \hat{h}_j | \Psi \rangle = \sum_{j}^{N} \langle \delta\chi_j | \hat{h}_j | \chi_j \rangle \tag{A.2}
$$

follows from an analogous calculation.

$$
\begin{aligned}
\langle \delta\Psi | \frac{1}{r_{jk}} | \Psi \rangle &= \int \mathrm{d}\mathbf{x}_1 \cdots \mathrm{d}\mathbf{x}_N \frac{1}{N!} \sum_{\sigma\in S_N} \sum_{l}^{N} \delta\chi^*_{\sigma(l)}(\mathbf{x}_l) \prod_{m\neq l}^{N} \chi^*_{\sigma(m)}(\mathbf{x}_m) \frac{1}{r_{jk}} \times \\
&\quad \sum_{\pi\in S_N} \mathrm{sgn}(\pi) \prod_{n}^{N} \chi_{\pi(n)}(\mathbf{x}_n) \\
&= \int \mathrm{d}\mathbf{x}_1 \cdots \mathrm{d}\mathbf{x}_N \sum_{\sigma\in S_N} \sum_{l}^{N} \delta\chi_l(\mathbf{x}_l)^* \prod_{m\neq l}^{N} \chi^*_m(\mathbf{x}_m) \frac{1}{r_{jk}} \prod_{n}^{N} \chi_{\sigma(n)}(\mathbf{x}_n) \\
&= \int \mathrm{d}\mathbf{x}_1 \cdots \mathrm{d}\mathbf{x}_N \sum_{\sigma\in S_N} \sum_{l}^{N} \Bigg\{ \delta_{lj}\delta\chi^*_j(\mathbf{x}_j)\chi^*_k(\mathbf{x}_k) \frac{1}{r_{jk}} \chi_{\sigma(j)}(\mathbf{x}_j)\chi_{\sigma(k)}(\mathbf{x}_k) \times \\
&\quad \prod_{m\neq j,k}^{N} \chi^*_l(\mathbf{x}_l)\chi_{\sigma(l)}(\mathbf{x}_l) + \\
&\quad \delta_{lj}\chi^*_j(\mathbf{x}_j)\delta\chi^*_k(\mathbf{x}_k) \frac{1}{r_{jk}} \chi_{\sigma(j)}(\mathbf{x}_j)\chi_{\sigma(k)}(\mathbf{x}_k) \prod_{m\neq j,k}^{N} \chi^*_m(\mathbf{x}_m)\chi_{\sigma(m)}(\mathbf{x}_m) \Bigg\}
\end{aligned}
$$

The term proportional to $(1-\delta_{lj})(1-\delta_{lk})$ in the third line has been eliminated using equation (2.33).

$$
\begin{aligned}
&= \int \mathrm{d}\mathbf{x}_j \mathrm{d}\mathbf{x}_k \Big\{ \delta\chi_j^*(\mathbf{x}_j)\chi_k^*(\mathbf{x}_k)\frac{1}{r_{jk}}\chi_j(\mathbf{x}_j)\chi_k(\mathbf{x}_k) - \\
&\quad \delta\chi_j^*(\mathbf{x}_j)\chi_k^*(\mathbf{x}_k)\frac{1}{r_{jk}}\chi_j(\mathbf{x}_j)\chi_k(\mathbf{x}_j) + \\
&\quad \chi_j^*(\mathbf{x}_j)\delta\chi_k^*(\mathbf{x}_k)\frac{1}{r_{jk}}\chi_j(\mathbf{x}_j)\chi_k(\mathbf{x}_k) - \\
&\quad \chi_j^*(\mathbf{x}_j)\delta\chi_k^*(\mathbf{x}_k)\frac{1}{r_{jk}}\chi_j(\mathbf{x}_k)\chi_k(\mathbf{x}_j) \Big\} \\
&= \langle \delta\chi_j\chi_k | \frac{1}{r_{12}} | \chi_j\chi_k \rangle + \langle \chi_j\delta\chi_k | \frac{1}{r_{12}} | \chi_j\chi_k \rangle - \\
&\quad \langle \delta\chi_j\chi_k | \frac{1}{r_{12}} | \chi_k\chi_j \rangle - \langle \chi_j\delta\chi_k | \frac{1}{r_{12}} | \chi_k\chi_j \rangle
\end{aligned}
\tag{A.3}
$$

A.2 SCF program for the quantum harmonic oscillator

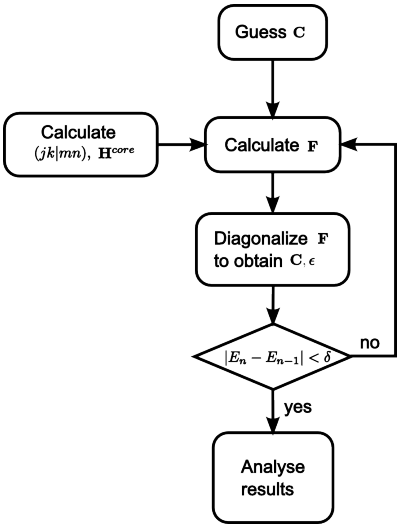

Figure A.1: Sketch of the algorithm used for the quantum harmonic oscillator

The program is implemented using the C programming language. As mentioned before the eigenfunctions are used as basis functions. These are orthonormal so that the algorithm reduces to the one sketched in A.1. The basis functions

$$\phi_n(r) = \frac{1}{\sqrt{2^n n! \sqrt{\pi}}} \exp\left\{-\frac{1}{2}r^2\right\} H_n(r) \tag{A.4}$$

are by construction eigenfunction of the one particle part of the Hamiltonian

$$\hat{h} = \frac{1}{2}\Delta + \frac{1}{2}r^2. \tag{A.5}$$

For convenience, the circular frequency ω is taken to be unity. Therefore, H^{core} is diagonal and has the form

$$H^{core}_{jk} = \delta_{jk} E_j = \delta_{jk}\left(j + \frac{1}{2}\right). \tag{A.6}$$

The two electron integrals are given by

$$\begin{aligned}(jk|mn) &= \int \mathrm{d}r_1 \mathrm{d}r_2 \phi^*_j(r_1)\phi_k(r_1)\frac{\mathrm{erf}(r_{12})}{r_{12}}\phi^*_m(r_2)\phi_n(r_2) \\ &= \mathrm{cst}\int \mathrm{d}r_1 \mathrm{d}r_1 \exp\left\{-r_1^2 - r_2^2\right\} H_j(r_1)H_k(r_1)\frac{\mathrm{erf}(r_{12})}{r_{12}}H_m(r_2)H_n(r_2) \\ &= \mathrm{cst}\int \mathrm{d}r_1 \mathrm{d}r_1 \exp\left\{-2r_1^2 - 2r_2^2\right\} H_j(r_1 + r_2)H_k(r_1 + r_2)\times \\ &\quad \frac{\mathrm{erf}(2|r_2|)}{2|r_2|}H_m(r_1 - r_2)H_n(r_1 - r_2),\end{aligned} \tag{A.7}$$

with

$$\text{cst} = \sqrt{\frac{1}{2^j j!\sqrt{\pi}}}\sqrt{\frac{1}{2^k k!\sqrt{\pi}}}\sqrt{\frac{1}{2^m m!\sqrt{\pi}}}\sqrt{\frac{1}{2^n n!\sqrt{\pi}}}. \tag{A.8}$$

Using the relations

$$\begin{aligned} H_n(r) &= (-1)^n \sum_{k_1+2k_2=n} \frac{(-1)^{k_1+k_2} n!}{k_1! k_2!} (2x)^{k_1} \\ H_n(r_1 + r_2) &= \sum_k \binom{n}{k} H_k(x)(2y)^{n-k} \end{aligned} \tag{A.9}$$

and

$$\begin{aligned} \int \mathrm{d}r r^n \exp\left\{-2r^2\right\} &= 2^{-n/2-3/2}\Gamma\left(\frac{n}{2}+\frac{1}{2}\right) \\ \int \mathrm{d}r r^n \frac{\operatorname{erf}(2|r|)}{|r|} \exp\left\{-2r^2\right\} &= \frac{2^{-n/2-1/2}}{\pi}\left(1+(-1)^n\right)\Gamma\left(\frac{1}{2}+\frac{n}{2}\right) \times \\ &\quad {}_2F_1\left(\frac{1}{2}, \frac{1}{2}+\frac{n}{2}, \frac{3}{2}, -2\right) \end{aligned} \tag{A.10}$$

the two electron integral (A.7) can be evaluated. All routines for the evaluation of (A.9), (A.10) and (A.7) are implemented in `twoElecIntErf.c`. The values of the hypergeometric function ${}_2F_1$ are needed only for discrete values of n. Thus, they are tabulated. The routines for the SCF procedure are implemented in `scf.c` and `uhf.c` for restricted and unrestricted Hartree-Fock calculations. With the routines from `scf.c` only ground state calculations are possible. Calculations with arbitrary occupation of the orbitals are possible using `uhf.c`. Both cases are limited to 12 basis functions. The two electron integrals (A.7) are expanded into a sum of integral expressions. The results of these integrals have alternating signs. When using more than 12 basis functions, the largest terms are of the order of 10^{20} whereas the result is of the order of 1. The `double` data type of C provides about 16 decimal digits accuracy. Thus, for more then 12 basis functions the values of the two electron integrals are wrong.